Mitochondrial Complex I and ROS control synapse function through opposing pre- and postsynaptic mechanisms

Bhagaban Mallik[1], C. Andrew Frank[1,2]

[1]Department of Anatomy and Cell Biology, University of Iowa Carver College of Medicine, Iowa City, IA, 52242, USA

[2]to whom correspondence should be addressed

andy-frank@uiowa.edu, @CAndrewFrank

SUMMARY

Neurons require high amounts energy, and mitochondria help to fulfill this requirement. Dysfunctional mitochondria trigger problems in various neuronal tasks. Using the *Drosophila* neuromuscular junction (NMJ) as a model synapse, we previously reported that Mitochondrial Complex I (MCI) subunits were required for maintaining NMJ function and growth. Here we report tissue-specific adaptations at the NMJ when MCI is depleted. In *Drosophila* motor neurons, MCI depletion causes profound cytological defects and increased mitochondrial reactive oxygen species (ROS). But instead of diminishing synapse function, neuronal ROS triggers a homeostatic signaling process that maintains normal NMJ excitation. We identify molecules mediating this compensatory response. MCI depletion in muscles also enhances local ROS. But high levels of muscle ROS cause destructive responses: synapse degeneration, mitochondrial fragmentation, and impaired neurotransmission. In humans, mutations affecting MCI subunits cause severe neurological and neuromuscular diseases. The tissue-level effects that we describe in the *Drosophila* system are potentially relevant to forms of mitochondrial pathogenesis.

Keywords: homeostatic plasticity; mitochondria; Mitochondrial Complex I; *Drosophila*; *ND-20L*; Mito-GFP; rotenone; NACA; *sod2*; ROS

INTRODUCTION

Neurons have vast energy needs. These needs are primarily satisfied by healthy pools of mitochondria [1,2]. Mitochondria generate energy through the action of the ATP synthase complex in the electron transport chain [3,4]. They also perform complementary functions, including maintaining calcium homeostasis [5,6], promoting cell survival [7], triggering reactive oxygen species (ROS) signaling [8], stimulating lipid synthesis [9], and regulating innate immunity [10]. For energy-driven neurons, it is thought that the primary role of mitochondria is to provide ATP. It is less understood how other mitochondrial functions contribute to the regulation of normal neurophysiology. It is also not well understood how neural tissues or synaptic sites cope when they are challenged with a loss of mitochondria. Genetic models can help to address these puzzles.

Mitochondrial Complex I (MCI) (NADH ubiquinone oxidoreductase) is an essential part of the electron transport chain and ATP production. MCI consists of 42 distinct subunits. Much of our understanding about MCI derives from systemic analyses of its assembly. Studies have been performed on Complex I components from diverse organisms, including *Neurospora crassa* and *Drosophila melanogaster*. Those studies demonstrate that discrete MCI subunits are ancient; indeed, there are few differences between these MCI models from simple organisms and the corresponding human and bovine orthologs [11-14]. For *Drosophila melanogaster*, 13/14 of the core MCI subunits are present, as are the remaining 28 accessory subunits [12].

In humans, MCI dysfunction has been linked to diseases such as Leigh syndrome, mitochondrial myopathy, and encephalomyopathy, as well as forms of stroke [15-18]. On a cellular level, MCI dysfunction can cause the demise of neurons and muscles; these phenotypes are typically attributed to defects in ATP production [19,20]. However, in addition to the ATP production defects, mutations affecting MCI subunit components are also associated with excess mitochondrial ROS. Normally, ROS accumulation can be neutralized by the cellular antioxidant system [21]. But if that system becomes overwhelmed, there can be consequences for cells and organ systems – including progressive neurodegeneration and seizures for the nervous system [22-24]. On the level of synapses, it is possible that MCI loss triggers severe molecular consequences, and it is also possible that excess ROS plays a role.

In a previous study, we depleted MCI function at the *Drosophila* neuromuscular junction (NMJ). Our data suggested fundamental synaptic functions for MCI [13]. Here we expand upon that work, mostly taking advantage of RNAi-mediated depletion of the nuclear DNA-encoded *NADH dehydrogenase subunit 20* (*ND-20L*) gene, a homolog of human NDUFS7. We also scrutinize loss-of-function mutants of other MCI subunits and pharmacological inhibition of MCI. Our collective data

show that MCI depletion causes *Drosophila* phenotypes reminiscent of mitochondrial diseases, such as progressive degeneration of muscle and presynaptic cytoskeleton, excess ROS production, loss of mitochondria and alteration in mitochondrial morphology.

On single-tissue levels, we were surprised to find that there were opposite effects on synapse activity in the presynaptic motor neurons vs. the postsynaptic muscles. MCI dysfunction in *Drosophila* motor neurons causes profound cytological phenotypes, but there are no significant functional phenotypes. This appears to be because neuronal mitochondrial ROS triggers an adaptive response, demonstrated visually by active zone enhancement. Based on our data, this ROS-driven enhancement of active zones occurs through at least two processes, 1) regulation of calcium flux from intracellular stores (ER) and mitochondria; and 2) use of glycolysis as an alternative energy source. By contrast, postsynaptic depletion of MCI and the associated elevation of muscle ROS triggers a destructive response: disruption of NMJ morphology and the Dlg-Spectrin scaffold that would normally be critical for normal active zone-receptor apposition. To our knowledge, these cellular and molecular mechanisms of MCI deficiency have not previously been elucidated at synapse-specific or tissue-specific levels.

RESULTS

Depletion of MCI affects mitochondrial integrity in multiple *Drosophila* synaptic tissues

In prior work, we reported impairments in neuromuscular junction (NMJ) synapse development and function when Mitochondrial Complex I (MCI) is depleted [13]. To understand those results better, we examined mitochondria by microscopy. We used the GAL4/UAS system to express a *UAS-Mito-GFP* transgene [25] in *Drosophila* tissues. Concurrently, we used tissue-specific GAL4 drivers alone (as controls) or GAL4 drivers + *UAS-ND-20L[RNAi]* to deplete *ND-20L* gene function by RNA interference, as previously published [13]. With these tools, we made qualitative observations of mitochondrial morphology (Fig. 1), and then we quantified those observations in subsequent analyses.

In motor neurons, the Mito-GFP signal localized to the neuropil of the ventral nerve cord (Fig.1: A-A′, B-B′). In control neurons, the neuropil mitochondria had a filamentous appearance. By contrast, *ND-20L*-depleted neurons had punctate and clustered mitochondria. (Fig. 1E-E′, F-F′). We examined mitochondria in the motor axons that innervate proximal and distal NMJs (Fig. 1C-C′, D-D′, G-G’, H-H’). The proximal segment A2 axons had abundant mitochondria in all cases (Fig. 1C-C’, G-G’). However, for the distal segment A5 axons, *ND-20L* depletion elicited an obvious decrease in mitochondria number (Fig. 1D-D,′ H-H,′). This A2 vs. A5 discrepancy was consistent with

prior work by others examining defects in mitochondrial trafficking dynamics: distal sites can show phenotypes more prominently [26,27].

We hypothesized that fewer mitochondria in the A5 axon might correlate with a neurotransmission defect at the NMJ. Yet by NMJ electrophysiology, we found no significant differences in the evoked amplitude compared to the control NMJs in the distal segment A5 (Fig. 1I-K). These data matched our prior examination of MCI at the A2 and A3 segments of the NMJ, where neuronal impairment of MCI was not sufficient on its own to reduce evoked NMJ neurotransmission [13].

In muscle, we observed an array of mitochondrial phenotypes. As with neurons, there were clustered mitochondria when *ND-20L* gene function was depleted (Fig. 1L-M). Additionally, there was a tissue-level phenotype: *ND-20L*-depleted muscles were developed, but they looked disorganized and fragmented, with oblong-shaped nuclei in the muscle syncytia (Fig. 1L-M). This phenotype could explain why we previously observed that muscle impairment of MCI was sufficient to reduce evoked NMJ neurotransmission [13].

To examine the mitochondria at presynaptic NMJ release sites, we used the motor neuron GAL4 driver to label NMJ boutons with Mito-GFP. For image analysis, we marked the presynaptic membrane boutons with anti-HRP immunostaining. Control NMJs contained abundant and large clusters of mitochondria in synaptic boutons, but by comparison, *ND-20L[RNAi]* boutons contained small clusters and few mitochondria (Fig. 1N-P). We measured the mitochondrial volume in a 3-D stack and compared it to the synaptic volume (Fig. 1Q-S). The Mito-GFP signal occupied a sizeable proportion of the bouton volume in controls (~30%), but this value was significantly diminished in *ND-20L*-depleted animals (~10%) (Fig. 1S). Collectively, our data suggest that the depletion of *ND-20L* by RNAi leads to abnormal mitochondrial clustering in the neuronal cell body and muscle – as well as losses of distal axon and synaptic mitochondria.

Loss of MCI phenocopies loss of Mitofusin

The cell-level ND-20L-depletion phenotypes were reminiscent of *Drosophila* mutants impairing mitochondrial dynamics [26,28]. Therefore, we re-examined MCI-depleted mitochondria, this time additionally impairing genes known to mediate mitochondrial fusion and fission. Mitofusin 1 (Mfn1) and Mitofusin 2 (Mfn2) are GTPases that regulate outer mitochondrial membrane fusion [29,30]. The *Drosophila* gene encoding the Mitofusin homolog is called *marf*. Dynamin-related protein 1 is a GTPase that regulates mitochondrial fission. In *Drosophila*, this factor is encoded by the gene *drp1* [31]. Previous work reported that defective fusion results in fragmented mitochondria, while defective fission can lead to enlarged mitochondria [32]. We used RNAi-mediated knockdown constructs for each of these genes.

As before, we observed that wild-type motor neurons had filamentous and oval mitochondria, while *ND-20L* depleted neurons had fewer and smaller clustered mitochondria in the ventral nerve cord (VNC) (Fig. 2A) and axons (Fig. 2B). Knockdown of the fusion gene *marf* phenocopied *ND-20L* loss, revealing small mitochondria in motor neurons, while knockdown of the fission gene *drp1* yielded filamentous mitochondria (Fig. 2A). Simultaneously depleting motor neurons of *marf* and *ND-20L* did not show any additive defect in mitochondrial appearance in the ventral nerve cord (VNC) and axons (Figs. 2A, B). This result could mean that the two genes share a common process to regulate mitochondrial fusion. By contrast, depleting *drp1* and *ND-20L* simultaneously yielded punctate mitochondria. This result likely means that that the punctate *ND-20L* mitochondrial phenotypes (potential fusion phenotypes) are epistatic to *drp1* loss (Fig. 2A, B). We measured mitochondrial branch length from skeletonized images of the mitochondria (Skeletonize3D, ImageJ plugin). Control and *drp1* knockdown showed normal mitochondrial branch length, but knockdown of *ND-20L* or *marf* – or knockdowns using combinations of each – exhibited short branch length (Fig. 2C, Table 1).

To quantify mitochondria in axons, we counted Mito-GFP positive puncta in distal A5 motor axons labeled by anti-GFP. Control axons and *drp1*-depleted axons contained abundant mitochondria (Fig. 2D, Table 1). By contrast, any gene manipulation or combination targeting *ND-20L* or *marf* resulted in diminished numbers of mitochondrial clusters (Fig. 2D, Table 1).

We extended the analysis to NMJ terminals. We counted Mito-GFP clusters in presynaptic boutons apposed by postsynaptic densities, labeled by anti-Discs Large 1 (Dlg1) (Figs. 2E-M). The results matched our earlier observations (Figs. 1N-S). Control NMJs and *drp1*-depleted NMJs contained numerous mitochondrial clusters per bouton (Figs. 2E, M). However, *ND-20L*-depleted boutons contained few mitochondria, and this was phenocopied by *marf*[RNAi] (Fig. 2E-M, Table 2). Collectively, these results suggest that *Drosophila ND-20L* (and hence MCI) contributes to normal mitochondrial fusion, likely in conjunction with the Mitofusin homolog, Marf.

Mitochondrial Reactive Oxygen Species Contribute to Synaptic Phenotypes

Several studies have demonstrated that Complex I loss results in high levels of mitochondrial reactive oxygen species (ROS) [33-37]. This means that excess ROS could be contributing to the cytological and mitochondrial fusion phenotypes that we have described.

We checked if we could observe mitochondrial ROS (superoxide) in living *Drosophila* tissue and if ROS levels corresponded to Complex I function (Fig. S1). We used a commercially available fluorescent mitochondrial superoxide indicator, MitoSOX (MitoSOX™, trademarked by ThermoFisher, Materials and Methods) [38-40]. With MitoSOX, we observed mitochondrial superoxide

in many tissues. There was a baseline level of ROS in controls (Fig. S1A, E, I, J, Table 3), and the level was greatly increased in *ND-20L*-deficient motor neuron cell bodies and muscle (Fig. S1B, F, I; J, Table 3).

Next, we tested if ROS scavengers could reverse the high Mito-SOX fluorescence levels in *ND-20L*-deficient tissues. We fed a pharmacological scavenger, N-Acetyl Cysteine Amide (NACA) [41-43] to *Drosophila* larvae (Materials and Methods). We also used a transgene, *UAS-sod2* [44], to express a superoxide dismutase enzyme. Both successfully diminished the high levels of mitochondrial ROS that resulted from *ND-20L* depletion at the NMJ, and both worked in muscle and neurons (Fig. S1C, D, G-J, Table 3).

We wondered if ROS scavengers could reverse mitochondrial phenotypes caused by loss of MCI. We considered *UAS-ND-20L[RNAi]* knockdown phenotypes. Co-expressing *UAS-sod2* or rearing larvae with NACA suppressed the mitochondrial morphology defects in the ventral nerve cord of *ND-20L*-depleted animals; it also restored axonal loss of mitochondria (Fig S2A-D, Table 4). To test an additional MCI manipulation, we knocked down *Drosophila ND-30* (homologous to human *NDUFS3*) in motor neurons. As with *ND-20L*, depleting *ND-30* in motor neurons yielded punctate mitochondria in the ventral nerve cord, but the addition of *UAS-sod2* restored a wild-type, filamentous mitochondrial morphology (Fig. S2A, C). Similarly, loss of *ND-30* gene function in neurons depleted A5 axonal mitochondria and this phenotype was also reversed by *UAS-sod2* transgenic expression (Fig. S2B, D, Table 4).

Because of the links between MCI and mitochondrial fusion, we considered whether a *marf* loss of function could also yield high levels of neuronal ROS (Fig. S3). It did – both *marf* and *ND-20L* loss-of-function conditions showed high levels of mitochondrial superoxide in motor neuron cell bodies (Fig. S3A-D, A'-D', M, Table 3); in motor axons (Fig. S3E-H, E'-H', N, Table 3); and at NMJ sites (Fig. S3I-L, I'-L', O, Table 3). These ROS phenotypes were not confined to genetic manipulations. We made similar observations when MCI was impaired pharmacologically by feeding rotenone to developing larvae (Fig. S3, Table 3). In the case of rotenone, the amount of mitochondrial ROS in the boutons was high, but it was not increased as much as with the genetic manipulations (Fig. S3K, O, Table 3).

Finally, because the distal A5 motor axons accumulated high levels of ROS when subjected to these insults, we examined them for synaptic vesicle trafficking defects. We immunostained for Cysteine String Protein (CSP), a DNAJ-like co-chaperone and synaptic vesicle-associated protein (Cysteine string protein: CSP). *ND-20L* depletion caused aberrant accumulation of CSP in the A5 motor axons; and this defect was suppressed upon motor neuron transgene expression of *UAS-sod2* or feeding animals with NACA (Fig. S4A-L, Table 5).

ROS scavengers did not reverse all mitochondrial abnormalities. Expressing *UAS-sod2* in the *UAS-ND-20L[RNAi]* or *UAS-marf[RNAi]*-depletion backgrounds did not restore mitochondrial clusters to motor neuron terminals (Fig. 2E-M, Table 2). For the remainder of the study, we used scavengers as complementary tools to test which MCI-loss phenotypes were likely due to mitochondrial ROS.

Loss of MCI subunits impairs synaptic cytoskeletal stability

ROS can modulate the cytoskeleton, either through redox modification of cytoskeletal proteins or by altering pathways that regulate cytoskeletal organization [45]. To test whether the mitochondrial defects and abnormal accumulation of ROS were associated with the altered synaptic cytoskeleton, we labeled synaptic boutons with an anti-Futsch antibody (Fig. 3). Futsch is a *Drosophila* MAP1B homolog that associates with microtubules [46].

In motor neuron Gal4-control and *UAS-sod2* overexpression larvae, Futsch organized in periodic loops, as expected from previous characterizations [46] (Fig.3A-B, Table 5). But in *ND-20L* depleted larvae, the anti-Futsch staining showed a significant reduction in microtubule loops (Figure 3C, Table 5). These *ND-20L* phenotypes were suppressed by motor neuron expression of *UAS-sod2* or by raising animals on food containing 0.5 mM NACA (Fig. 3D-E, Table 5). These data indicate that loss of MCI regulates cytoskeletal architecture due to excessive accumulation of ROS in neurons.

Modest neurotransmission phenotypes after motor neuron-specific loss of MCI or marf

Given the cytological phenotypes after neuronal MCI loss, it was puzzling that there seemed to be little to no electrophysiological consequence at NMJs ([13] and Fig. 1J). We probed this finding, this time depleting motor neurons of *marf* and/or *ND-20L* gene function. We recorded spontaneous miniature postsynaptic potentials (mEPSP) and evoked excitatory postsynaptic potentials (EPSP).

Phenotypes were normal-to-mild (Fig. S5). For both *ND-20L[RNAi]* and *marf[RNAi]*, there were small, but statistically significant decreases in mEPSP amplitude (Fig. S5A-C, G, Table 6). But for *ND-20L[RNAi]*, evoked events (EPSP) and calculated quantal content (QC) were at control levels (Fig. S5A-B, H-I, Table 6). For neuronal *marf[RNAi]*, those measures were near-normal, with a slight decrease in EPSP amplitude (Fig. S5C, H, Table 6) and a slight increase in QC (Fig. S5I, Table 6). Finally, for a double *ND-20L[RNAi]* + *marf[RNAi]* knockdown condition in neurons, we observed a small, but statistically significant decrease in EPSP amplitude.

Synaptic phenotypes caused by mitochondrial dysfunction might be masked until synapses are challenged with extreme conditions, like high frequency stimulation [47,48]. Therefore, we challenged neuronally *ND-20L*-depleted *Drosophila* NMJs in several ways (Fig. S6). First, we lowered recording saline [Ca^{2+}] to 0.15 mM, which is roughly one order of magnitude lower than physiological calcium. In low calcium, the motor neuron-driven *ND-20L[RNAi]* NMJs had slightly smaller evoked potentials compared to driver controls, but the numerical reduction was not statistically significant (Fig. S6A-C, Table 7). Next, we lowered extracellular [Ca^{2+}] even further, to 0.1 mM, which yielded a mix of successful EPSP firing events and failures. Failure analyses revealed an increase in failure rate at the neuronally depleted *ND-20L[RNAi]* NMJs compared to control animals (Fig S6D, Table 7), demonstrating a decreased probability of release. Failure rates in 0.1 mM calcium were restored to baseline levels when *ND-20L*-depleted larvae were raised in a media containing NACA or genetically expressing *sod2* in motor neurons (Fig S6D, Table 7), indicating that a sensitivity to low calcium could be related to ROS levels.

Finally, we checked if forms of short-term neuroplasticity were affected by *ND-20L* loss in motor neurons. For two different extracellular [Ca^{2+}] conditions (0.4 to 1.5 mM), we did not observe any significant changes in paired-pulse ratios (Figs. S6E-J, Table 7). Likewise, we did not see any notable depreciation of evoked neurotransmission over the course of high frequency stimulus trains in high calcium (Figs. S6K-P, Table 7). Collectively, these data suggest that there might be a small effect on NMJ physiology due to defective mitochondrial fusion, and the defect could be sensitive to low levels of extracellular calcium – but the aggregate data also indicate that neuronal mitochondrial defects alone do not drastically affect NMJ neurotransmission.

Loss of MCI in neurons controls the level and distribution of the active zone to stabilize synaptic strength

We wondered how synapse might evade severe dysfunction, despite loss of mitochondria in the motor neurons. One possibility is that *ND-20L* loss/MCI impairment could trigger a form of functional homeostatic compensation of the NMJ. Another idea is that the mitochondrial ATP generated is superfluous at the NMJ – and that any energy-intensive functions that mitochondria support could be redundantly covered by glycolysis. These models are not mutually exclusive, and for any scenario, mitochondrial ROS downstream of defective MCI could be a candidate signal. Recent findings have demonstrated that ROS intermediates, mitochondrial distribution, and mitochondrial trafficking all affect development of the *Drosophila* NMJ [45,49,50].

We imaged the presynaptic active zone apparatus in neuronally-depleted *ND-20L[RNAi]* flies. Third-instar larval active zones showed a decrease in BRP puncta density per unit area in *ND-*

20L-depeleted NMJs compared to control NMJs (Fig.4A-C, G, H-I, Table 8). But they also showed a robust enhancement phenotype: in *ND-20L*-depleted animals, we found a 40% increase in active zone (BRP) immunofluorescence signal per unit area, compared to control (Fig. 4 A-C, F, H-I, Table 8), by laser scanning confocal microscopy. This result was intriguing because NMJ active zone enhancements (or changes in active zone sub-structure) have been proposed by other labs to be molecular correlates of forms of homeostatic plasticity and potentiation of neurotransmitter release [51-55]. This raised the possibility that the NMJs evade severe dysfunction through a form of synaptic homeostasis.

As an independent test, we impaired MCI pharmacologically. To do this, we raised larvae on rotenone-spiked food; and we also incubated wild-type fillet preparations with 500 µM of rotenone for extended time. For both cases, we observed significant increases in BRP protein at the presynaptic active zones (Fig S7A-U, Table 9). For the extended incubation, the fillet preparations required sufficient rotenone incubation time (six hours) and an intact motor nerve to show the active zone enhancement (Fig. S7U, Table 9). This latter result suggested that delivery of active zone material required either trafficking time and/or fully intact neuroanatomy.

Next, we checked if the enhanced active zone signal by was triggered by excess mitochondrial ROS in motor neurons. Indeed, we found that the *ND-20L*-depletion active zone enhancements were fully reversed by ROS scavengers, either by raising larvae in food containing NACA or by neuronally expressing *UAS-sod2* (Fig. 4 D-G, Table 8).

Finally, we assessed synapse function. As with our prior recordings, evoked postsynaptic potentials at the NMJ were not significantly changed by *ND-20L* depletion in motor neurons. But interestingly, scavenging mitochondrial ROS in the *ND-20L[RNAi]* neuronal depletion background with *UAS-sod2* revealed a small decrease in NMJ excitation, compared to controls (Fig. 4J-P, Table 8). This could mean that mitochondrial ROS is helping to maintain synaptic activity. Consistently, neuronal expression of *UAS-sod2* did not restore mitochondrial clusters to the NMJ after *ND-20L* gene function depletion (Fig. 4Q-U, Table 8; like Fig. 2H), meaning that the synaptic sites were still deficient in mitochondria. Our data support a model in which neuronal ROS (nROS) triggers active zone enhancement functional compensation when MCI is limiting (Fig. 4V-X, Table 8).

Neuronal MCI subunits stabilize synaptic strength in conjunction with intracellular calcium signaling proteins

Recent work described a mechanism for local calcium uptake into mitochondria that drives ATP production to maintain synaptic function [56]. The process is governed by the mitochondrial calcium

uniporter (MCU) and its accessory EF-hand MICU proteins [56]. Beyond this role for mitochondrial calcium, there are also known roles for core synaptic functions like vesicle cycling [57,58].

To test if mitochondrial or neuronal calcium could be involved in maintaining synapse function at the NMJ, we acquired genetic reagents to examine depressed MCU function in conjunction with depressed MCI. We also used pharmacological reagents to inhibit release of intracellular sources of calcium, like those from the Ryanodine Receptor (RyR) and the IP_3 receptor (IP_3R) of the endoplasmic reticulum (ER) [59], as well as a genetic reagent that we previously used at the NMJ to deplete IP_3 signaling (*UAS-IP$_3$-sponge*) (Fig. 5A-D). For this set of experiments, we used the *ND-20L* neuronal knockdown condition as a sensitized genetic background (Fig. 5E-T, Table 10).

We observed no significant differences in EPSP amplitudes when we impaired *mcu* function (Table 10). Similarly, we did not observe deficits in baseline synaptic activity by blocking RyR and IP_3R, alone or in conjunction with *ND-20L*[RNAi] (Fig. 5E-H, Q-T, Table 10). However, when we concurrently impaired a combination of *ND-20L*, *mcu*, and ER calcium store channels, we observed marked decreases in evoked amplitude (Fig. 5K-L, S, Table 10). These results are consistent with a model in which mitochondrial Ca^{2+} uptake, MCU activation, and ER (store) Ca^{2+} efflux combine to stabilize synaptic strength.

If this idea were correct, then it should also be possible to chelate cytoplasmic calcium in a neuronal *ND-20L[RNAi]* background and reveal neurotransmission defects. Direct application of the membrane-permeable chelator BAPTA-AM, followed by a wash to remove chelator residing in the saline, had no significant effect on baseline neurotransmission parameters (DMSO carrier + wash). But in the *ND-20L[RNAi]* background, BAPTA-AM + wash significantly diminished evoked potentials, compared to mock-treated (DMSO + wash) NMJs. (Fig.5 M-T, Table 10).

To check if these effects on neurotransmission correlated with effects on active zone protein accumulation, we also conducted anti-Brp immunostaining experiments (Fig. S8). As before, neuronal knockdown of *ND-20L* gene function triggered a marked, compensatory increase in presynaptic active zone material that was readily apparent by confocal microscopy (Figs. S8A, C, I, Table 11). But this increase was reversed when combined with *mcu* gene function knockdown and pharmacological blockade of store calcium release channels (Figs. S8G-I, Table 11). Together, our data indicate that loss of MCI subunits in neurons sensitizes synapses to decreases in intracellular calcium.

A combination of mitochondria, glycolysis, and the TCA Cycle stabilizes NMJ function

Neuronal calcium handling and MCU play roles in NMJ stability that are uncovered by loss of MCI at the NMJ. Downstream of calcium handling, a logical hypothesis is that synaptic energy would

play a role [56]. If this were the case, would mitochondria be the sole energy source? Alternatively, in the absence of full mitochondrial function, could glycolysis theoretically substitute, as a homeostatic (or redundant) means for staving off synapse dysfunction?

We tested these ideas by limiting glycolysis as an energy source in two ways: 1) swapping out sucrose and trehalose in our recording saline in favor of 2-deoxy-D-glucose (a non-glycolytic sugar; (Fig. 6A); 2) addition of lonidamine (LDA) to the saline to acutely inhibit hexokinase (Fig. 6A). Control recordings with these conditions showed little effect on baseline physiology (Fig. 6A, D, F, H-J, Table 12). However, when Mitochondrial Complex I was impaired neuronally through *ND-20L[RNAi]* in combination with inhibition of glycolysis, there was a drop in evoked neurotransmission (Fig. 6C, E, G, H-J, Table 12). This correlated with a failure to increase active zone material after *ND-20L* gene knockdown (Fig. 6K-Q, Table 12). These results match the idea that a combination of mitochondrial function or glycolysis can work to maintain normal levels of NMJ output.

We continued this line of investigation genetically. We acquired RNA interference-based transgenes to target five genes involved in *Drosophila* glycolysis or subsequent ATP generation in the Citric Acid (TCA) Cycle: *hexokinase A (hex-A)*, *hexokinase C (hex-C)*, *Citrate (Si) Synthase I*, *Isocitrate dehydrogenase* (*Idh*), and *Succinyl-coenzyme A synthetase α subunit 1* (*Scsα1*). We knocked down these genes neuronally, either alone or in combination with *ND-20L[RNAi]* (Figs. S9 and S10). Neuronal impairment of *hex-C* had no effect on baseline neurotransmission, but *hex-A* impairment reduced it (Figs. S9A-E, Table 13). Impairment of the TCA Cycle enzymes on their own had little-to-no effect on baseline neurotransmission (Fig. S9A, F-H, Table 13). However, concurrent impairment of *ND-20L* and most of these genes significantly blunted neurotransmission, with the exception being *hex-C* (Figs. S9I-N, Table 13). Collectively, the data suggest that MCI works in conjunction with – or redundantly to – alternative energy-generating pathways to support normal levels of neurotransmission. In the case of the hexokinases, *Drosophila hex-A* seems more important for this process than *hex-C*.

We also assayed active zone material accumulation. The results mirrored the neurotransmission tests: as before, neuronal *ND-20L[RNAi]* impairment elicited enhanced active zone material (Fig. S10, Table 14). But concurrent neuronal impairment of *ND-20L* and any of the glycolysis or TCA Cycle genes reversed this active zone enhancement (Fig. S10, Table 14).

MCI subunits in muscle are required for proper synapse development

We previously reported that impairments of MCI diminish *Drosophila* NMJ growth [13]. The roles of MCI in specific tissues for this developmental function were unclear. For the present study, we tested for tissue-specific roles of MCI in NMJ development. To visualize NMJ boutons, we co-stained

larval fillets with anti-Horseradish Peroxidase (HRP) a presynaptic membrane marker, and anti-Discs Large (Dlg), a postsynaptic density marker [60,61].

On a coarse level, MCI loss in muscle (*BG57-Gal4 > UAS-ND-20L[RNAi]*) caused a severe reduction in average bouton size, a decrease in bouton number, a notable decrease in Dlg expression, and a bouton "clustering" phenotype (Fig. 7 A-B), reminiscent of what we previously reported [13]. To quantify these observations, we measured bouton number, muscle area, and branch number per muscle in the third-instar larval NMJ synapses (Table 15). We found that *ND-20L* muscle knockdown resulted in a significant reduction in all these parameters compared to controls (Fig 7J-L, U-V, Table 15).

In contrast to muscle knockdown, pan-neuronal or motor neuron-specific knockdown of *ND-20L* showed slight NMJ overgrowth phenotypes (Fig. 7F-L, Table 15). As was the case with the active zone enhancement associated with neuronal *ND-20L* knockdown (Fig. 4), this NMJ overgrowth could represent a developmental mechanism to stave off dysfunction caused by missing neuronal mitochondria. Taken together, our NMJ immunostaining results indicated to us that blunted NMJ growth due to MCI loss was likely due to muscle MCI dysfunction.

We tested if the NMJ undergrowth phenotypes could be due to the increased levels of mitochondrial reactive oxygen species in muscle (mROS) (Fig. S1F). If that idea were correct, then the undergrowth phenotypes should be reversed if mitochondrial mROS were scavenged. Consistent with this idea, bouton number and synaptic undergrowth phenotypes were fully restored to wild-type levels when the *ND-20L[RNAi]* muscle knockdown animals also had *UAS-sod2* transgenically expressed in the muscles (Fig. 7C, J-L, R, Table 15). They were also restored to wild-type levels when muscle *ND-20L* knockdown animals were raised on food containing the antioxidant N-acetyl cysteine amide (NACA) (Fig. 7J-L, Table 15). By contrast, none of these NMJ growth parameters were restored to wild-type levels if scavengers *UAS-sod1* or *UAS-catalase* were misexpressed in the muscle (Fig. 7D-E, J-L, Table 15). SOD1 (cytosol) and Catalase (peroxisomes) localize to different compartments than SOD2 (mitochondrial matrix). These results likely indicates that a scavenger needs to access the proper mitochondrial compartment for rescue.

Loss of MCI and mROS in muscle disorganize NMJ postsynaptic densities

The muscle Dlg-Spectrin network functions as an organizing scaffold for synaptic assembly [61,62]. Dysregulation of this network can lead to an aberrant muscle subsynaptic reticulum (SSR) [61]. Therefore, one possible target of excess mROS in the absence of MCI function is Dlg. Dlg is the fly homologue of PSD-95/SAP97/PSD-93, and it is a member of the membrane-associated guanylate

kinase (MAGUK) family of NMJ scaffolding proteins [61]. It is present both within presynaptic boutons and in the portion of the SSR closest to the bouton.

Using the same antibodies detailed above (anti-Dlg and anti-HRP), we used a high magnification to examine at the postsynaptic densities closely. By confocal immunofluorescence, Dlg area was significantly reduced when *ND-20L* was depleted postsynaptically by[RNAi] (Fig. 7M-U, Table 15). To quantify the relative Dlg area, we measured Dlg area with respect to HRP (Relative Dlg area = Dlg area minus HRP area) in type 1b boutons at muscle 6/7 of the A2 hemisegment (Fig. 7U). Compared with the control synapses, *ND-20L* knockdown resulted in a significant reduction in the relative Dlg area (Fig 7M-U, Table 15). Consistently, the relative α-Spectrin area was also reduced when *ND-20L* was depleted in muscle (Fig. S11A-F, Table 5).

Next, we scavenged mROS, and then we examined the postsynaptic densities. The relative Dlg and α-Spectrin areas were restored to wild-type levels when animals were grown in a media containing NACA (*ND-20L[RNAi]/+; BG57-Gal4*/+ with NACA) or genetically expressing *UAS-sod2* in the muscle (*UAS-sod2/ND-20L[RNAi]; BG57-Gal4/BG57-Gal4*) (Fig.7R, U, Table 15; Fig. S11D-F, Table 5). By contrast, Dlg levels were not restored while expressing other scavengers in the muscle, encoded by *UAS-sod1* and *UAS-catalase* transgenes (Fig. 7S-U, Table 15). We conclude that depletion of MCI subunits in the muscle disables postsynaptic density formation via the formation of mitochondrial reactive oxygen species intermediates.

The postsynaptic density (PSD-95/Dlg) has been shown to cluster glutamate receptors at the SSR [63]. Our results raised the possibility that glutamate receptor clusters could be disrupted when *ND-20L* was depleted in the muscle (Fig. 8). To test this idea, we simultaneously immunostained NMJs with antibodies against Brp (neuron, presynaptic active zone) and glutamate receptor clusters (muscle). In controls, these pre- and postsynaptic structures were directly apposed to one another (Fig. 8A, G). But when *ND-20L* gene function was depleted, we observed “missing” GluRIIA and GluRIII receptor clusters (Fig. 8 B, F, H, K, Table 5), i.e., Brp puncta without apposed glutamate receptors. These lack of apposition phenotypes were fully reversed by raising the larvae with NACA or genetically expressing *UAS-sod2* in the muscle (Fig. 8 D-F, I-K, Table 5). Together, our data indicate that loss of MCI subunit in the muscle (*ND-20L*) disrupts several aspects of the postsynaptic density organization, and these disruptions are likely due to the accumulation of mROS in the muscle.

Loss of MCI subunits in muscle diminishes evoked NMJ neurotransmission through postsynaptic mROS

Mitochondria and reactive oxygen species influence presynaptic vesicle release and plasticity at synapses. This has been shown in diverse model systems like flies, mice, and worms [49,50,64-66]. In our prior work, we identified an NMJ neurotransmission defect when MCI function is impaired [13], but based on our current study, that defect does not seem like it was dependent upon MCI's neuronal functions (Figs. 1, 4, 5, 6). Therefore, we turned to analyzing postsynaptic muscle MCI and mROS to check if these parameters influenced neurotransmission.

We performed sharp electrode electrophysiological recordings of miniature and evoked excitatory postsynaptic potentials (mEPSP and EPSP) at NMJ muscle 6, hemisegment A2. We also used average mEPSP and EPSP values to estimate quantal content (QC) for each NMJ. For the most part, mEPSP values remained steady (Figs. 9A-E, Table 16), with some exceptions. The starkest phenotypes came in terms of evoked amplitudes (Figs. 9A-D, F), sometimes due to changes in QC (Fig. 9G) or combinatorial changes in both mEPSP (Fig. 9E) and QC (Fig. 9G).

Evoked synaptic vesicle release (EPSP) was significantly reduced when *ND-20L* was depleted in muscles by RNAi (Fig. 9A, F, Table 16). That reduction was reversed after scavenging mitochondrial ROS in the muscle. Indeed, transgenic muscle-driven *sod2* gene expression suppressed the *ND-20L[RNAi]* phenotype, but expression of the *catalase* and sod1 did not (Fig. 9A, F, Table 16). Next, we tested if feeding a ROS scavenger to developing larvae would reverse the same neurotransmission defect. Carrier feeding alone (10% EtOH) did not affect evoked neurotransmission, nor did it influence the neurotransmission loss caused by *ND-20L[RNAi]* (Fig. 9B, F, Table 16). Feeding larvae 0.5 mM NACA successfully reversed the phenotype, while the nonspecific additive curcumin had no effect (Fig. 9B, F, Table 16).

We also checked different MCI manipulations. First, we examined hemizygous *ND-30$^{EY03664/Df}$* genetic mutants. As with muscle-driven *ND-20L[RNAi]*, the *ND-30* mutant NMJs had blunted evoked neurotransmission, but this defect was successfully reversed by ROS scavengers (Fig. 9C, Table 16). We also impaired MCI pharmacologically, by feeding larvae 50 µM rotenone (or 0.5% DMSO carrier control), similar to conditions we previously published [13]. As with the prior study, rotenone blunted neurotransmission (Fig. 9D, Table 16), but this effect was ameliorated by a genetic background overexpressing *UAS-sod2* in the muscle (Fig. 9D, Table 16). Consistent with prior experiments *UAS-catalase* and *UAS-sod1* were not effective.

Finally, we performed behavioral experiments on *ND-20L* and *ND-30[RNAi]* and mutant animals. Consistent with the electrophysiological recordings, muscle-depleted (by RNAi) and mutant animals showed severe defects in crawling ability. The abnormal crawling behavior was rescued by expressing a *sod2* transgene in the muscle or feeding the larvae in a media containing NACA (Fig. 9H, Table 17). By contrast, neuronal depletion of *ND-20L* in larvae did not show any significant

crawling defects (Fig. 9H, Table 17). Together, our data suggest that excess ROS accumulation in muscle (mROS) diminishes baseline synaptic physiology when MCI activity is lost, and it also triggers aberrant crawling behavior.

DISCUSSION

We uncovered novel aspects of NMJ synapse biology controlled by Mitochondrial Complex I (MCI). Global impairment of MCI causes profound cytological phenotypes in synaptic tissues (Figs. 1-3) [13]. By examining mitochondria directly, we discovered shared phenotypes between MCI loss and loss of the *Drosophila* mitofusin, Marf (Fig. 2). Additionally, with MCI loss, we noted an enhancement of mitochondrial reactive oxygen species (ROS, Fig. S1), consistent with prior work [33-37].

Unexpectedly, these perturbations spur functionally opposite responses in presynaptic neurons vs. postsynaptic muscles. In motor neurons, MCI loss and mitochondrial ROS appear to trigger a compensatory response, where the underlying cytological problems are offset by an increase in active zone material, resulting in normal levels of evoked excitation (Fig. 4). This process requires known intracellular calcium signaling components (Fig. 5). It also appears to require energy stores because loss of glycolysis – which may function as a supplemental energy source to mitochondria – abrogates the presynaptic compensation (Fig. 6). By contrast, in the muscle, MCI loss and mitochondrial ROS trigger a destructive response, where there is a disassembly of the postsynaptic density (Fig. 7). This disassembly correlates with mis-apposition of pre- and postsynaptic structures (Fig. 8) and defective neurotransmission (Fig. 9).

Disruption of mitochondrial dynamics

Energy is needed for normal levels of synaptic transmission [2]. Intuitively, a loss of synaptic mitochondria should blunt transmission. Several labs have implicated mitochondrial dynamics in *Drosophila* synapse function, including mitochondrial fission (Dynamin related protein 1, Drp1 [48]), fusion (Mitofusin/dMarf [28]), trafficking (Miro and Milton [47,67,68]), or quality control (Pink and Parkin [69-72]). Additionally, it has been established from various model organisms such as flies, worms, and mice that any misregulation in mitochondrial distribution could affect synaptic activity [48,56,73,74]. Adding to that work, we uncovered synaptic transmission and developmental phenotypes after depletion of Mitochondrial Complex I (MCI) at the NMJ [13].

Separate and apart from those studies, ROS has been studied in the context of mitochondrial dysfunction [75]. Excess ROS can trigger mitochondrial calcium uptake and subsequently trigger apoptosis or degeneration of neurons or neural support cells [76,77]. MCI deficiency elevates ROS

levels, and this process can promote the fragmentation of mitochondria in cells like fibroblasts [78]. Collectively, the prior work suggest that mitochondrial ROS can impinge upon cell survival and mitochondrial dynamics. Our study expands upon these results and supports the idea that MCI has roles at synaptic sites. Lack of MCI in neurons causes loss of mitochondria at synaptic terminals (Fig. 1). This defect is linked to defective mitochondrial fusion (Fig. 2), which is essential to maintain mitochondrial integrity [79,80].

A form of presynaptic homeostatic plasticity triggered by ROS?

ROS has been linked to short-term synaptic plasticity in *Drosophila* [50], as well as long-term potentiation (LTP) in mammals [81-83]. Here, we uncovered a role for ROS in augmentation of active zone material when MCI is impaired in neurons. This finding could be considered a form of homeostatic plasticity: an increase in active zone components likely drives potentiated release to compensate for defective baseline synaptic transmission, which would be expected after the loss of an energy source like mitochondria.

Homeostatic augmentations of active zone material have been observed at the *Drosophila* NMJ. For example, *rab3* mutants have an increase in active zone material to offset decreased synapse growth [84]. Additionally, ROS has been shown to be an obligate signal in *Drosophila* to maintain fundamental properties in both pre- and postsynaptic compartments, including at the NMJ [50]. In our study, we observe an increase in active zone intensity (Fig. 4), which could overlap with mechanisms uncovered in those prior studies. Or it could be consistent with a form of homeostatic plasticity at the *Drosophila* NMJ called Presynaptic Homeostatic Potentiation (PHP). PHP is initiated when the activity of postsynaptic glutamate receptors is impaired. This decreases quantal size. The synapse detects the impairment, and muscle-to-nerve signaling drives an increase in presynaptic glutamate release [85,86]. This happens in part through an increase in influx of calcium into the neuron through Ca_V2 voltage-gated calcium channels [85,87-90]. PHP coincides with an increase in the size of the readily releasable pool (RRP) of synaptic vesicles [91-94] and increases in active zone protein content [51,53,95]. The general model is that these modifications drive the neuron to release more glutamate, offsetting the initial synaptic challenge.

Could the excess mitochondrial ROS that is caused by the loss of Complex I be triggering the same or overlapping homeostatic mechanisms? It is possible. Quenching presynaptic ROS by expression of *sod2* or by feeding flies NACA led to a reversion of active zone material back down to the control levels (Fig. 4E). Under ideal conditions, control levels of active zone material would support normal neurotransmission (Fig. 4A, J). However, when combined with presynaptic *ND-20L* loss

(already depleting synaptic mitochondria; Figs. 1O, 2G), there is a loss in neurotransmission capacity (Fig. 4M).

The molecular underpinnings of this mitochondrial-loss-induced homeostatic plasticity are unknown, but prior work might offer clues. One possibility is that *sod2* changes the redox status of the entire cell, which could potentially affect active zone components [81]. Another possibility is that ROS could alter the release of calcium from intracellular stores such as ER; and in turn, this could induce calcium signaling to mitochondria, which would contribute to the formation of ATP and subsequent vesicle fusion [56,57]. Consistent with this idea, we observed a reduced synaptic strength at the terminals after simultaneous blockade of calcium release and import from ER stores to mitochondria through genetic or pharmacological manipulations (Fig. 5). But notably, the link would not have to be a direct one. Indeed, a recent study indicated that activity-driven mitochondrial Ca^{2+} uptake does not depend on the ER as a source of Ca^{2+} to maintain normal synaptic strength [56].

Loss of MCI in muscle and subsequent ROS accumulation diminish synaptic excitation

Little is known about what role postsynaptic ROS plays in regulating synaptic plasticity at the NMJ. It is unlikely that ROS is an abstract signal that triggers wholesale destruction. It likely has specific targets. There are clues from previous work. For example, ROS signaling plays direct roles in the activity-dependent structural plasticity of motor neurons and postsynaptic dendrites [50]. Additionally, postsynaptic ROS plays critical roles in dendritic development. In *Drosophila*, ROS appears to act as a developmental plasticity signal to regulate the size of the dendritic arbors. [96].

It is slightly surprising that the NMJ fails to compensate for a lack of MCI function in the muscle. This is because the NMJ employs multiple retrograde signals to stabilize function [97]. One hypothesis is that MCI deficiency and ROS interfere with important muscle-to-nerve signals normally required for maintaining NMJ setpoint function. Some of these signals are required to correct acute challenges (minutes) to NMJ function. Some of the best characterized are: Bone Morphogenetic Protein (BMP) signaling [98-100]; the Insomniac (adaptor)-Cul3 (ubiquitin ligase)-Peflin (substrate) signaling complex [101]; and the endosomal recycling molecules class II PI3 kinase (PI3K) and Rab11 [102]. Additionally, the field has uncovered instructive signaling molecules from the muscle that maintain robust neurotransmission, including: muscle-secreted Semaphorin-2b [103]; and Target of Rapamycin (TOR) [104,105]. Future studies can address whether these or similar targets are substrates of negative ROS regulation in the muscle.

The roles of ROS in muscle are less understood in terms of synapse regulation and function. In this study, we showed that excess ROS is sufficient to affect the organization of postsynaptic densities (Fig. 7), ionotropic glutamate receptor clusters (Fig. 8), and spectrin cytoskeleton (Fig.

S11) in the muscle. The correlated uncoupling of pre- and postsynaptic structures seems to be responsible for neurotransmission defects (Fig. 9), and it likely coincides with broader structural instability [62,106]. These phenotypes are reminiscent of other *Drosophila* mutant phenotypes showing a degenerative NMJ (e.g., [62,106-108]). Consistent with a model of degeneration, we found behavioral defects in locomotion (Fig. 9).

Despite these many defects that result from muscle depletion of MCI, we successfully rescued many structural and functional defects by culturing animals in an antioxidant-rich media (0.5mM NACA) or through muscle expression of *UAS-sod2*. This is interesting because it points to mitochondrial ROS as a signal of interest in the manifestation of synapse dysfunction. In subsequent work, we will take advantage of the *Drosophila* neurogenetic toolkit to identify specific targets. In turn, these targets could be informative about how MCI dysfunction manifests in mitopathies.

RESOURCE AVAILABILITY

Lead Contact

The lead contact for this study is Dr. C. Andrew Frank (andy-frank@uiowa.edu).

Materials Availability

Dr. Frank's laboratory uses the fruit fly *Drosophila melanogaster* as a model organism. Consistent with ethical conduct of research, the lab maintains *Drosophila* stocks that it generates and publishes, as well as useful precursors and derivatives of those stocks. These stocks are available to researchers who make requests to Dr. Frank – or to the appropriate original source – and they are shipped promptly.

Data and Code Availability

Consistent with the Data Sharing Policy for NIH-funded research, Dr. C. Andrew Frank's laboratory will share data related to this study. The lab will share final data through publication of summary figures or tables. In addition, a large amount of final data derives from performing electrophysiological recordings or synapse imaging experiments and then performing subsequent analyses. Those experiments yield raw data in electronic form. Therefore, in addition to publishing final data, the lab will share raw data and related materials with researchers who make requests to Dr. Frank (andy-frank@uiowa.edu). No original coding was required to execute this study.

Acknowledgments

We acknowledge the Developmental Studies Hybridoma Bank (University of Iowa, USA) for antibodies used in this study and the Bloomington Drosophila Stock Center (Indiana University, Bloomington, USA) for fly stocks. We thank members of the Frank lab for their helpful comments and discussions in this study. BM was supported in part by NIH/NINDS grants to CAF (NS085164, NS130108, and NS136753). Collectively, the work was supported by those same NIH/NINDS grants, as well as funds from the University Carver College of Medicine to CAF.

Author contributions

BM and CAF designed the research; BM performed the research; BM and CAF analyzed the data; BM and CAF wrote the paper.

Declarations of interests

The authors declare no competing financial interests.

SUPPLEMENTAL INFORMATION

Document S1:

- Supplemental Figures S1-S11 and legends.

Document S2:

- Tables 1-17: Summary data for graphs in all Figures and Supplemental Figures.
- Table 18: Detailed information about reagents and materials for items described in the STAR METHODS section.

FIGURE LEGENDS

Figure 1: MCI-depleted flies harbor fewer mitochondria at neuromuscular junctions

Mitochondrial morphology and trafficking defects in the ventral nerve cord, distal axons, and boutons. RNAi lines and controls were crossed to a motor neuron driver (*D42-GAL4*) and a mitochondrial marker (*UAS-mitoGFP*). (A-A′), (B-B′), (C-C′) and (D-D′) represent control ventral nerve cord (VNC), a magnified section of VNC, proximal (A2) and distal (A5) axons, respectively. These tissues exhibit regular mitochondrial clusters in the soma and axons. (E-E′), (F-F′), (G-G′) and (H-H′) represent *ND-20L* knocked down ventral nerve cord (VNC), a magnified section of VNC, proximal (A2) and distal (A5) axons, respectively. Mitochondria are abnormally clustered in *ND-20L[RNAi]* in the ventral nerve cord and distal segments of A5 axons. *ND-20L[RNAi]* yields fewer mitochondria in the distal segments when compared to the proximal segments. (I-J) Representative electrophysiological traces showing evoked potentials of *mitoGFP, D42-Gal4* × *UAS-ND-20*[RNAi] larvae at the A5 hemisegment of muscle 6/7 synapse. Scale bars for EPSPs (mEPSP) are x=50 ms (1000 ms) and y= 10 mV (1 mV). Fewer mitochondria at the presynaptic A5 hemisegment did not affect evoked NMJ excitation. K. Quantification showing EPSP amplitude at NMJ 6/7 in control (*D42-Gal4/+*; EPSP: 19.99 mV ± 2.53, n=6) and RNAi-depleted animals (*ND-20L[RNAi] /+;D42-Gal4/+* ;EPSP: 16.88 mV ± 1.21, n=9). (L-M) Representative images showing mitochondria morphology in control and RNAi-depleted animals in muscle. Mitochondria in *ND-20L[RNAi]*-depleted larvae are clustered compared to the control larvae. (N-Q) *ND-20L[RNAi]* contains almost no mitochondria in boutons when co-stained with pre- (HRP) or post-synaptic markers (Discs Large, Dlg). (A-H′, L-M, N-O) Scale bar: 10 µm. (P) Quantification showing the number of mitochondrial clusters at NMJ 6/7 in control (*D42-Gal4/+*; # clusters: 113.6 ± 11.97, n=7) and RNAi-depleted animals (*ND-20L[RNAi]/+; D42-Gal4/+*; # clusters: 30.33 ± 4.02, n=6). (Q-R) 3D rendered image showing the volume (µm^3) of mitochondria at NMJ 6/7 in RNAi knockdown larvae (*ND-20L[RNAi] /+; D42-Gal4/+ ;* 0.11 ± 0.01 µm^3, n=16) compared to the driver control animals (*D42-Gal4/+*; 0.29 ± 0.04 µm^3, n=14). (Q-R) Scale bar: 5 µm. (S) Quantification shows a significantly lower mitochondria volume in boutons at NMJ 6/7 in RNAi-depleted animals. ***p<0.0001 and ***p=0.0003 for mitochondrial clusters and volume, respectively. Statistical analyses based on Student's t-test. Error bars represent mean ± s.e.m.

Figure 2: Loss of *ND-20L* in motor neurons phenocopies a *marf* depletion

Mitochondrial morphology and trafficking defects in the ventral nerve cord and distal axons. To label neuronal mitochondria, *UAS-[RNAi]* lines and controls were crossed to a motor neuron driver (*D42-Gal4*) and a mitochondrial marker (*UAS-mitoGFP*). (A) Ventral nerve cord (VNC): *UAS-mitoGFP* and *drp1[RNAi]* exhibit normal mitochondrial organization, *ND-20L[RNAi]* and *marf*[RNAi] exhibit clustered mitochondria, *ND-20L[RNAi] ; marf[RNAi]* and *ND-20[RNAi]; drp1[RNAi]* doubles exhibit clustered mitochondria in the soma. The fluorescent images were skeletonized to measure mitochondrial branch length. (B) Comparison of a proximal axonal segment in A2 and a distal segment in A5. Distal segments of A5 axons in *ND-20L[RNAi]* and *marf[RNAi]* contain many fewer mitochondria than proximal segments. Knocking down *ND-20L[RNAi]* and *marf[RNAi]* together does not show an additive effect. (A-B) Scale bar: 10 µm. (C-D) Histogram showing mitochondrial branch length (µm) and number (μm^2 area of bouton) in VNC and axons of the third instar larvae in the indicated genotypes. (E-L) Representative images of the A2 hemisegment of muscle 6/7 NMJs in (E) *UAS-mito-GFP, D42-Gal4/+*, (F) *UAS-sod2/+; UAS-mito-GFP, D42-Gal4/+,* (G) *ND-20L[RNAi] /+; UAS-mito-GFP, D42-Gal4/+*, (H) *ND-20L[RNAi] /UAS-sod2;UAS-mito-GFP,D42-Gal4/+*, (I) *UAS-mito-GFP,D42-Gal4/marf[RNAi]* , (J) *UAS-sod2;UAS-mito-GFP,D42-Gal4/marf[RNAi]* , (K) *ND-20L[RNAi] /+;UAS-mito-GFP,D42-Gal4/marf[RNAi]* and (L) *ND-20L[RNAi] /UAS-sod2;UAS-mito-GFP,D42-Gal4/marf[RNAi]* larvae immunostained with antibodies against HRP (magenta) and GFP (mito-GFP:green) to label neurons and mitochondria. *ND-20L[RNAi]*- and *marf[RNAi]*-depleted animals harbor fewer mitochondria at the terminals as compared to control animals. Transgenic *UAS-sod2* rescued mitochondrial clustering defects. (E-L) Scale bar: 5 µm. (M) Histograms showing quantification of mitochondrial clusters at the NMJs in the indicated genotypes. ****p* <0.0001; ns, not significant. Statistical analysis based on one-way ANOVA followed by post-hoc Tukey's multiple-comparison test. Error bars represent mean ± s.e.m.

Figure 3: *ND-20L* depletion in motor neurons affects synapse stability

Representative confocal images of NMJ synapses at muscle 6/7 of (A-A′) *D42-Gal4* control, (B-B′) *UAS-sod2* overexpression (C-C′) *D42-Gal4*-driven *ND-20L*[RNAi] (*ND-20L[RNAi] /+; D42-Gal4/+*), (D-D′) *ND-20L* knockdown with NACA rescue (*ND-20L[RNAi] /+; D42-Gal4/+* +NACA), (E-E′) *ND-20L* knockdown with *UAS-sod2* (*UAS-ND-20L[RNAi]/UAS-sod2; D42-Gal4/+*). Each condition was double immunolabeled with 22C10 (anti-Futsch, magenta) and anti-HRP (green) antibodies. The motor neuron-depleted *ND-20L[RNAi]* larvae showed a decrease in the number of Futsch-positive loops as compared to the Gal4 control. Futsch-positive loops were significantly restored to the control number when *ND-20L*[RNAi] was raised in media containing NACA or genetically expressing *UAS-sod2* in the *UAS-ND-20L[RNAi]* background. Scale bar: 10 µm. (F) Histograms showing the percentage of Futsch-positive loops in the indicated genotypes. **p*=0.01 (Gal4 control vs *sod2* OE neuron), **p*=0.0008 (Gal4 control vs *ND-20L*[RNAi] neuron), ***p*=0.001 (*ND-20L*[RNAi] neuron vs *ND-20L*[RNAi] neuron + NACA) and ***p*=0.0005 (*ND-20L*[RNAi] neuron vs *sod2* neuron rescue). Statistical analysis based on one-way ANOVA followed by post-hoc Tukey's multiple-comparison test. Error bars represent mean ± s.e.m.

Figure 4: Neuronal ROS (nROS) controls active zone material levels at NMJs

(A) Representative images of the A2 hemisegment of muscle 6/7 NMJs in *UAS-mito-GFP, D42-Gal4/+*, (B) *UAS-sod2/+; UAS-mito-GFP, D42-Gal4/+* (C) *ND-20L[RNAi]/+; UAS-mito-GFP, D42-Gal4/+*, (D) *ND-20L[RNAi] /+; UAS-mito-GFP, D42-Gal4/+* with NACA and (E) *ND-20L[RNAi]/UAS-sod2; UAS-mito-GFP, D42-Gal4/+* larvae immunostained with antibodies against the active zone scaffold Bruchpilot (BRP:fire-LuT) to label the active zones. BRP levels are upregulated at the NMJs in *ND-20L*[RNAi] depleted flies, while overexpression of ROS scavenger *sod2* in the neuron or feeding the larvae with N-Acetyl L-cystine amide (NACA) restores BRP to the control level. (A-E) Scale bar: 2.5 µm. (F-G) Histograms showing quantification of BRP intensity (F) and density (G) in μm^2 area of bouton at muscle 6/7 in the genotypes mentioned above. At least 8 NMJs of each genotype were used for quantification. ***p <0.0001. Error bars denote mean ± s.e.m. Statistical analysis based on one-way ANOVA followed by post-hoc Tukey's multiple-comparison test (H-H′-I-I′). Representative confocal images of muscle 6/7 NMJs in the (H-H′) control (*D42-Gal4/+*) and (I-I′) motor neuron Gal4 driven *ND-20L[RNAi]* (*ND-20L[RNAi] /+; D42-Gal4/+*) immunostained with antibodies against Bruchpilot (BRP: magenta) and GluRIII (green) to label a glutamate receptor subunit. (H-H′-I-I′) Scale bar: 2.5 µm. There are no significant changes of GluRIII-BRP apposed clusters. At least 8 NMJs of each genotype were used for quantification (J-P). Representative traces, quantification of mEPSPs, EPSPs and quantal content in the indicated genotypes. Scale bars for EPSPs (mEPSP) are x=50 ms (1000 ms) and y= 10 mV (1 mV). EPSPs amplitudes were maintained in *ND-20L[RNAi]*-depleted flies due to induction of BRP; however, NMJ with *sod2* rescued *ND-20L[RNAi]* in neurons showed diminished evoked release when compared with *ND-20L[RNAi]*. Minimum 8 NMJs recordings of each genotype were used for quantification. *p < 0.05, ***p <0.0001; ns, not significant. Statistical analysis based on one-way ANOVA followed by post-hoc Tukey's multiple-comparison test. Error bars denote the standard error of the mean. (Q) Representative images of the A2 hemisegment of muscle 6/7 NMJs in *UAS-mito-GFP, D42-Gal4/+*, (R) *UAS-sod2/+; UAS-mito-GFP, D42-Gal4/+* (S) *ND-20L[RNAi] /+; UAS-mito-GFP, D42-Gal4/+*, and (T) *ND-20L[RNAi]/UAS-sod2; UAS-mito-GFP,D42-Gal4/+* larvae immunostained with antibodies against HRP (magenta) and GFP (mito-GFP:green) to label neurons and mitochondria. *ND-20L*-depleted and *sod2*-rescued *ND-20L*[RNAi] animals harbor fewer mitochondria at the terminals than control animals. (Q-T) Scale bar: 5 µm. (U) Histograms showing quantification of mitochondrial clusters in the above-indicated genotypes. (V-X) Schematic illustration showing ROS (magenta) levels, BRP (grey) and mitochondria (red) number in the indicated genotypes. At least 8 NMJs of each genotype were used for quantification. ***p<0.0001. Error bars represent mean ± s.e.m. Statistical analysis based on one-way ANOVA followed by post-hoc Tukey's multiple-comparison test.

Figure 5: Loss of MCI subunit induces ER-mediated calcium release to maintain evoked neurotransmission at the NMJs

(A-D) Schematics illustrating the role of IP_3 receptor (IP_3R), Ryanodine receptor (RyR) in the endoplasmic reticulum, mitochondrial calcium uniporter Complex (MCU), Ca_v2 calcium channel and synaptic vesicles at the presynaptic nerve terminal. The IP3 and Ryanodine receptors were blocked pharmacologically by using IP_3R antagonist Xestospongin C or presynaptically expressing *UAS-IP$_3$-Sponge* and RyR antagonist Dantrolene, while *mcu*[RNAi] was used to block the Mitochondrial calcium uniporter complex. (E-P) Representative traces of mEPSPs and EPSPs in (E) pan-neuronal Gal4 control (*elaV(C155)-Gal4/*+), (F) pan-neuronal Gal4 control (*elaV(C155)-Gal4/*+) with an acute application (10 minutes) of 20 µM Xestospongin C and 10 µM Dantrolene, (G) pan-neuronal Gal4 driven *ND-20L*[RNAi] (*elaV(C155)-Gal4)/+;ND-20L[RNAi] /*+), (H) pan-neuronal Gal4-driven *ND-20L*[RNAi] (*elaV(C155)-Gal4/+;ND-20L[RNAi] /*+) with 20 µM Xestospongin C and 10 µM Dantrolene, (I) pan-neuronal Gal4 driven UAS-*IP3-Sponge.m30* with an acute application of 10 µM Dantrolene (*elaV(C155)-Gal4)/+;ND-20L[RNAi] /+;UAS-IP3-Sponge.m30/*+), (J) pan neuronal Gal4 driven *mcu*[RNAi] with 20 µM Xestospongin C and 10 µM Dantrolene (*elaV(C155)-Gal4)/+;mcu[RNAi] /+),* (K) pan-neuronal *mcu[RNAi]* + *ND-20L*[RNAi] with 20 µM Xestospongin C and 10 µM Dantrolene and(*elaV(C155)-Gal4)/+;mcu[RNAi] /ND-20L[RNAi]*) and (L) pan neuronal *UAS-IP3-Sponge.m30* + *mcu[RNAi]* + *ND-20L*[RNAi] with 10 µM Dantrolene (*elaV(C155)-Gal4/+;ND-20L[RNAi] /mcu[RNAi] ;UAS-IP$_3$-Sponge.m30/*+), (M) Pan neuronal Gal4 (*elaV(C155)-Gal4/*+) with DMSO, (N) pan neuronal Gal4 (*elaV(C155)-Gal4/*+) with 20 µM BAPTA-AM, (O) pan-neuronal Gal4 driven *ND-20L*[RNAi] (*elaV(C155)-Gal4)/+;ND-20L[RNAi] /*+) with DMSO and (P) pan neuronal Gal4 driven *ND-20L*[RNAi] (*elaV(C155)-Gal4)/+;ND-20L[RNAi] /*+) with 20 µM BAPTA-AM. Scale bars for EPSPs (mEPSP) are x=50 ms (1000 ms) and y= 10 mV (1 mV). Note that EPSPs amplitudes were reduced in pan-neuronal Gal4 driven *mcu[RNAi]* + *ND-20L*[RNAi] with an acute exposure of 20 µM Xestospongin C, 10 µM Dantrolene or *UAS-IP$_3$-sponge.m30* + *mcu[RNAi]* + *ND-20L*[RNAi] with 10 µM Dantrolene and pan-neuronal Gal4 driven *ND-20L*[RNAi] with 20 µM BAPTA-AM. (Q-T) Histograms showing average mEPSPs, EPSPs amplitude, and quantal content in the indicated genotypes. A minimum of 8 NMJs recordings of each genotype were used for quantification. ***p* < 0.05 (EPSP and QC: *ND-20L*[RNAi] neuron + DMSO, wash vs *ND-20L*[RNAi] neuron + BAPTA-AM, wash), *p < 0.05, ***p*=0.001, ****p* <0.0001; ns, not significant. Statistical analysis based on one-way ANOVA followed by post-hoc Tukey's multiple-comparison test. Error bars represent mean ± s.e.m.

Figure 6: Loss of MCI subunit induces glycolysis and regulates levels of active zone materials to stabilize synaptic strength

(A) Schematic illustrations showing steps of glucose metabolism and ATP production during glycolysis and TCA cycle in the cell. (B-G) Representative traces of mEPSPs and EPSPs in (B) pan-neuronal Gal4 control (*elaV(C155)-Gal4/*+ with DMSO), (C) pan-neuronal Gal4 control (*elaV(C155)-Gal4/*+) with an acute application (30 minutes) of 150 µM Lonidamine (LDA) (D) pan-neuronal Gal4 driven *ND-20L*[RNAi] (*elaV(C155)-Gal4)/+; ND-20L[RNAi]* /+ with DMSO), (E) pan-neuronal Gal4 driven *ND-20L*[RNAi] (*elaV(C155)-Gal4)/+; ND-20L[RNAi]/*+) with 150 µM Lonidamine, (F) pan-neuronal Gal4 control (*elaV(C155)-Gal4/*+) and HL3 containing 2-Deoxy-D-glucose and (G) pan-neuronal Gal4 driven *ND-20L*[RNAi] (*elaV(C155)-Gal4)/+; ND-20L[RNAi]* /+) with HL3 containing 2-Deoxy-D-glucose. Scale bars for EPSPs (mEPSP) are x=50 ms (1000 ms) and y= 10 mV (1 mV). The EPSPs amplitudes were reduced in pan-neuronal Gal4-driven *ND-20L*[RNAi] with an acute exposure of 150 µM Lonidamine (LDA) or pan-neuronal Gal4-driven *ND-20L*[RNAi] in HL3 containing 2-Deoxy-D-glucose for 30 minutes. However, we saw a reduction in mEPSP amplitudes when incubated in HL3 containing 2-Deoxy-D-glucose for 30 minutes in pan-neuronal Gal4-driven *ND-20L[RNAi]* -depleted larvae compared to the control animals. (H-J) Histograms showing average mEPSPs, EPSPs amplitude, and frequencies in the indicated genotypes. A minimum of 8 NMJ recordings of each genotype were used for quantification. ,***p*=0.003 (mEPSP amplitude: *elaV(C155)-Gal4/*+2-Deoxy-D-glucose vs *elaV(C155)-Gal4)/+;ND-20L[RNAi]* / +2-Deoxy-D-glucose), ***p*=0.002 (EPSP amplitude: *elaV(C155)-Gal4/*+2-Deoxy-D-glucose vs *elaV(C155)-Gal4)/+;ND-20L[RNAi]* /+2-Deoxy-D-glucose),****p*=0.0001 (EPSP amplitude: *elaV(C155)-Gal4/*+LDA vs *elaV(C155)-Gal4)/+;ND-20L[RNAi]* / +LDA); ns, not significant. Statistical analysis is based on the Student's t-test for pairwise sample comparison. Error bars represent mean ± s.e.m. (K-P) Representative images of the A2 hemisegment of muscle 6/7 NMJs in the above-indicated genotypes immunostained with antibodies against the active zone scaffold bruchpilot (BRP:fire-LuT) to label the active zones. The BRP levels downregulated at the NMJs in pan-neuronal Gal4 driven *ND-20L*[RNAi] either incubated with 150 µM LDA or in HL3 containing 2-Deoxy-D-glucose for 30 minutes. (K-P) Scale bar: 5 µm. (Q) Histograms showing quantification of BRP intensity in μm^2 area of bouton at muscle 6/7 in the genotypes mentioned above. At least 8 NMJs of each genotype were used for quantification.****p*<0.0001 (BRP levels: *elaV(C155)-Gal4/*+DMSO vs *elaV(C155)-Gal4)/+;ND-20L[RNAi]/*+ +DMSO),***p*=0.008 (BRP levels: *elaV(C155)-Gal4/*+LDA vs *elaV(C155)-Gal4)/+;ND-20L[RNAi]* /+LDA), ****p*=0.0005 (BRP levels: *elaV(C155)-Gal4/*+2-Deoxy-D-glucose vs *elaV(C155)-Gal4)/+;ND-20L[RNAi]* /+2-Deoxy-D-glucose). Error bars denote mean ± s.e.m. Statistical analysis based on one-way ANOVA followed by post-hoc Tukey's multiple-comparison test.

Figure 7: *ND-20L* subunit in muscles is required to promote normal synapse growth

(A-I) Representative confocal images of NMJ synapses at muscle 6/7 of (A) Muscle-Gal4 control (*BG57-Gal4/+*), (B) Muscle Gal4 driven *ND-20L*[RNAi] (*ND-20L[RNAi] /+; BG57-Gal4/+*), (C) *sod2* muscle rescue (*UAS-sod2/ND-20L[RNAi] ; BG57-Gal4/BG57-Gal4*), (D) *sod1* muscle rescue (*UAS-sod1/ND-20L[RNAi] ; BG57-Gal4/BG57-Gal4*), (E) catalase muscle rescue (*UAS-cat/ND-20L[RNAi] ; BG57-Gal4/BG57-Gal4*), (F) Pan neuronal Gal4 control (*elaV(C155)-Gal4)/+*), (G) *elaV(C155)- Gal4)-Gal4* driven *ND-20L*[RNAi] (*elaV(C155)-Gal4/+; ND-20L[RNAi] /+*), (H) Motor neuron Gal4 control *(D42-Gal4/+)* and (I) *D42*-Gal4-driven *ND-20L*[RNAi] (*ND-20L[RNAi] /+; D42-Gal4/+*) double immunolabeled with Dlg (magenta) and HRP (green) antibodies. (A-I) Scale bar: 10 µm. The NMJ morphological defects in *ND-20L*[RNAi] were restored upon co-expression of *UAS-Sod2 in* muscle; however, it did not rescue with *UAS-sod1* or *UAS-catalase* transgene. (J-L) Histograms show the number of boutons, muscle area, and average NMJ length at muscle 6/7 of A2 hemisegment in the indicated genotypes. *p <0.05, *p=0.006 (# of boutons: Muscle *ND-20L*[RNAi] vs *sod2* muscle rescue), **p=0.0002 (# of boutons: Muscle *ND-20L*[RNAi] vs Muscle *ND-20L*[RNAi] +NACA), *p=0.009 (# of branches: Muscle Gal4 vs Muscle *sod2* OE), ***p=0.002 (# of branches: Muscle Gal4 vs Muscle *sod1* OE), *p=0.008 (# of branches: Muscle Gal4 vs Muscle *cat* OE), ***p=0.001 (Muscle Gal4 vs Muscle *ND-20L*[RNAi]), ***p<0.0001; ns, not significant. Statistical analysis based on one-way ANOVA with post-hoc Tukey's test for multiple and Student's t-tests for pairwise comparison. Error bars represent mean ± s.e.m. (M-T) Representative confocal images of boutons at the third instar larval NMJ synapse in (M) Muscle-Gal4 control (*BG57-Gal4/+*), (N) Muscle Gal4 driven *UAS-sod2* (*UAS-sod2/+; BG57-Gal4/+*), (O) *UAS-sod1* (*UAS-sod1/+; BG57-Gal4/+*), (P) *UAS-catalase* (*UAS-catalase/+; BG57-Gal4/+*) (Q) Muscle *ND-20L*[RNAi] (*ND-20L[RNAi] /+; BG57-Gal4* (R) *sod2* muscle rescue (*UAS-sod2/ND-20L[RNAi] ; BG57-Gal4/BG57-Gal4*), (S) *sod1* muscle rescue (*UAS-sod1/ND-20L[RNAi] ; BG57-Gal4/BG57-Gal4*) and (T) catalase muscle rescue (*UAS-cat/ND-20L[RNAi] ; BG57-Gal4/BG57-Gal4*) animals double immunolabeled with anti-HRP (green) and anti-Dlg (magenta) antibodies. (M-T) Scale bar: 5 µm. Note that the gross morphology of SSRs and immunoreactivity of Dlg were reduced in *ND-20L[RNAi]* animals. As mentioned, phenotypes were restored to wild-type level when *ND-20L*[RNAi] -depleted flies were reared in NACA or by genetically expressing *sod2* transgene in muscle. (U-V) Histograms showing normalized synaptic fluorescence of Dlg and bouton area in the indicated genotypes. *p <0.01, **p <0.001, ***p<0.0001; ns, not significant. Error bars represent mean ± s.e.m. Statistical analysis based on one-way ANOVA with post-hoc Tukey's test for multiple and Student's t-tests for pairwise comparison.

Figure 8: *ND-20L* subunit in muscle affects the organization of GluRs cluster in *Drosophila*.
Representative confocal images of boutons at third instar larval NMJ synapse in (A) Muscle-Gal4 control (*BG57-Gal4/*+), (B) Muscle *ND-20L*[RNAi] (*ND-20L[RNAi] /+; BG57-Gal4/*+), (C) Muscle Gal4 driven *UAS-sod2* (*UAS-sod2*/+*; BG57-Gal4/*+), (D) *ND-20L[RNAi] /+; BG57-Gal4/*+NACA) and (E) *sod2* muscle rescue (*UAS-Sod2/ND-20L[RNAi] ; BG57-Gal4/BG57-Gal4*) animals immunolabeled with active zone marker BRP (green) and anti-GluRIII (magenta) antibodies. Scale bar: 5 µm. Note that GluRIII apposed clusters with BRP are missing in the *ND-20L*[RNAi]-depleted animals (marked in arrow) compared to control. These phenotypes were restored to normal when *ND-20L*[RNAi]-depleted flies were reared in media containing NACA or genetically expressing *sod2* transgene in muscle. (F) Histograms showing quantification of the number of missing BRP-GluRIII apposed puncta per bouton in the indicated genotypes. (G-J) Similar phenotypes were observed when analyzed for BRP-GluRIIA apposed clusters in boutons. (K) Histograms showing quantification of the number of missing BRP-GluRIIA apposed puncta per bouton in the indicated genotypes. ***$p<0.0001$. Error bars represent mean ± s.e.m. Statistical analysis based on one-way ANOVA with post-hoc Tukey's test for multiple comparisons.

Figure 9: Loss of MCI subunits affects synaptic transmission via the formation of excess ROS in the muscle

(A) Representative traces of mEPSPs and EPSPs in muscle-Gal4 control (*BG57-Gal4/+*), muscle Gal4 driven *ND-20L*[RNAi] (*ND-20L[RNAi] /+; BG57-Gal4/+),* muscle *catalase* rescue (2X muscle-Gal4>*UAS-catalase/ND-20L*[RNAi] : *UAS-catalase/ND-20L[RNAi] ; BG57-Gal4/BG57-Gal4*), muscle *sod1* rescue (2X muscle-Gal4>*UAS-sod1/ND-20L*[RNAi] : *UAS-sod1/ND-20L[RNAi] ; BG57-Gal4/BG57-Gal4*), muscle *sod2* rescue (2X muscle-Gal4>*UAS-sod2/ND-20L*[RNAi] : *UAS-sod2/ND-20L[RNAi] ; BG57-Gal4/BG57-Gal4*) animals. Note that EPSPs amplitudes were reduced in *ND-20L[RNAi],* and the phenotype was restored to wild-type levels by expressing *sod2* transgene in the muscle but not with *sod1* and *catalase* transgenes. (B) Representative traces of mEPSPs and EPSPs in muscle Gal4 control (*BG57-Gal4/+*) larvae raised on 10% EtOH, *ND-20L* muscle[RNAi] (*ND-20L[RNAi] /+; BG57-Gal4/+*) raised on 10% EtOH, *ND-20L* muscle[RNAi] (*ND-20L[RNAi] /+; BG57-Gal4/+*) raised on 0.5mM curcumin, *ND-20L* muscle[RNAi] (*ND-20L[RNAi] /+; BG57-Gal4/+*) raised on 0.5mM NACA, (C) Representative traces of mEPSPs and EPSPs in *ND-30^{epgy}/df* mutants, *ND-30^{epgy}/df* mutants raised on 0.5 mM NACA and *UAS-sod2* muscle rescued *ND-30^{epgy}/df* mutant (*UAS-sod2/+; ND-30 (df), BG57-Gal4/ND-30^{epgy}*) animals. The EPSPs amplitudes were restored to wild type when muscle depleted *ND-20L*[RNAi] larvae were raised in food containing NACA or by *UAS-sod2* muscle overexpression in *ND-20L*[RNAi] depleted animals. (D) Representative traces of mEPSPs and EPSPs in muscle-Gal4 control (*BG57-Gal4/+*) larvae raised on DMSO, muscle Gal4 (*BG57-Gal4/+*) larvae raised on 50µM rotenone (complex I inhibitor), *UAS-catalase (UAS-catalase/+; BG57-Gal4/)*, *UAS-sod1(UAS-sod1/+; BG57-Gal4/),* and *UAS-sod2 (UAS-sod2/+; BG57-Gal4/+)* muscle over-expression animals raised on 50µM rotenone. The EPSPs amplitudes were suppressed in rotenone raised larvae overexpressing *UAS-Sod2* in muscle *(UAS-sod2/+; BG57-Gal4/)* due to its free radical scavenging activity. Scale bars for EPSPs (mEPSP) are x=50 ms (1000 ms) and y= 10 mV (1 mV). (E-G) Histograms showing average mEPSPs, EPSPs amplitude, and quantal content in the indicated genotypes. Minimum 8 NMJs recordings of each genotype were used for quantification. (H) Histogram representing crawling behavior (in cm) of the larvae in the indicated genotypes. Knocking down *ND-20L*[RNAi] or *ND-30*[RNAi] in muscle and *ND-30^{epgy}/df* mutants showed a severe defect in crawling behavior. The abnormal crawling behavior was rescued by expressing a *sod2* transgene in the muscle or rearing the larvae in a media containing NACA. Moreover, neuronally depleting *ND-20L* did not show any notable change in crawling defects. Minimum 10 animals were analyzed for crawling behavioral analysis. *p < 0.05 (mEPSP amplitude: Muscle *ND-20L*[RNAi] +10% EtOH vs Muscle *ND-20L*[RNAi] +0.5 mM NACA),**p=0.006 (mEPSP amplitude: *ND-30* mutant vs *N-30* mutant+0.5 mM NACA), *p=0.0004 (mEPSP amplitude: Muscle-Gal4+0.5% DMSO vs. Muscle *cat* OE+50mM rotenone),*p=0.039 (mEPSP

amplitude: Muscle Gal4+50mM rotenone vs Muscle *sod2* OE+50mM rotenone), **p*=0.001 (EPSP amplitude: Muscle *ND-20L*[RNAi] vs *sod2* muscle rescue),***p*=0.003 (EPSP amplitude: Muscle Gal4+10% EtOH vs Muscle *ND-20L*[RNAi] +0.5mM curcumin), ***p*=0.0004 (EPSP amplitude: Muscle *ND-20L*[RNAi] +10% EtOH vs Muscle *ND-20L*[RNAi] +0.5mM NACA), **p*=0.004 (EPSP amplitude: Muscle-Gal4+0.5% DMSO vs Muscle Gal4+50mM rotenone), *p=0.015 (EPSP amplitude: Muscle-Gal4+0.5% DMSO vs Muscle *cat* OE+50mM rotenone),***p*=0.015 (EPSP amplitude: Muscle-Gal4+0.5% DMSO vs Muscle *sod1* OE+50mM rotenone), ***p*=0.001 (QC*: ND-30* mutant vs *sod2* muscle rescue),***p*=0.003 (QC: Muscle Gal4+50mM rotenone vs Muscle *sod*2 OE+50mM rotenone), ***p*=0.0002 (Distance crawled: Muscle Gal4 vs Muscle *ND-30*[RNAi]), ****p* <0.0001; ns, not significant. Statistical analysis based on one-way ANOVA with post-hoc Tukey's test for multiple and Student's t-test for pairwise comparison.

TABLES

All tables contain raw data supporting the graphs in the figures and are housed in the supplementary section.

STAR METHODS

Experimental Model Details

Drosophila husbandry

Drosophila melanogaster was cultured on a standard cornmeal media containing molasses and yeast prepared according to the Bloomington *Drosophila* Stock Center (BDSC, Bloomington, IN) recipe. Fruit flies husbandry was performed according to standard practices [109]. As specified, larvae were raised at 18°C, 25°C, or 29°C in humidity-controlled and light-controlled Percival DR-36VL incubators (Geneva Scientific). Control,[RNAi] , and mutant animals were grown in media containing 0.5 mM curcumin (Sigma Aldrich), 0.5 mM N-acetyl cysteine amide (NACA) (Sigma Aldrich), or 50 µM rotenone (Sigma Aldrich) depending upon the experimental condition.

Drosophila stocks

w^{1118} was used as a non-transgenic wild-type stock. *UAS-IP$_3$-sponge* line (*UAS-IP$_3$-Sponge.m30*) was obtained from Dr. Masayuki Koganezawa's lab. The GAL4 drivers used in this study were $elav^{C155}$-Gal4, *Sca*-Gal4 and *BG57*-Gal4, *D42*-Gal4, and *OK371*-Gal4. Several *UAS-RNAi* and genetic mutant lines were obtained from the Bloomington *Drosophila* stock center (Table 18).

Method Details

Immunohistochemistry

Wondering third instar larvae were dissected and fixed on a sylgard Petri plate in ice-cold HL-3 and fixed in 4% paraformaldehyde in PBS for 30 minutes or in Bouin's fixative for 2 minutes as described earlier [110]. Briefly, larvae were washed with PBS containing 0.2% Triton X-100 (PBST) for 30 min, blocked for an hour with 5% normal goat serum in PBST, and incubated overnight in primary antibodies at 4°C followed by washes and incubation in secondary antibodies. Monoclonal antibodies: anti-Dlg (4F3), anti-DGluRIIA (8B4D2), anti-CSP (ab49), anti-Synapsin (3C11), anti-Futsch (22C10), anti-Bruchpilot (nC82) and anti-α-Spectrin (3A9) were obtained from the Developmental Studies Hybridoma Bank (University of Iowa, USA) and were used at 1:30 dilution. Rabbit anti-GFP (Abcam) was used at 1:200 dilutions. Anti-GluRIII (1:100) ([111]; Table 18) was gifted by Aaron DiAntonio (Washington University, St. Louis, U.S.A.). Fluorophore coupled secondary antibodies Alexa Fluor 488, Alexa Fluor 568 or Alexa Fluor 647 (Molecular Probes, ThermoFisher Scientific) were used at 1:400 dilution. Alexa 488 or 647 and Rhodamine conjugated anti-HRP were used at 1:800 and 1:600 dilutions, respectively. The larval preparations were mounted in VECTASHIELD (Vector Laboratories, USA) and imaged with a laser scanning confocal microscope (LSM 710; Carl Zeiss). All the images were processed with Adobe Photoshop 7.0 (Adobe Systems, San Jose, CA).

Confocal imaging, quantification, and morphometric analysis

Samples were imaged using a Carl Zeiss scanning confocal microscope equipped with 63×/1.4 NA oil immersion objective using separate channels with four laser lines (405, 488, 561, and 637 nm) at room temperature. The stained NMJ boutons were counted using anti-Synapsin or anti-HRP co-stained with anti-Dlg on muscle 6/7 of A2 hemisegment, considering each Synapsin or HRP punctum to be a bouton. At least 8 NMJs were used for bouton number quantification. For fluorescence quantifications of GluRs, Dlg, Brp, α-Spectrin, HRP, and CSP, all genotypes were immunostained in the same tube with identical reagents, then mounted and imaged in the same session. Z-stacks were obtained using identical settings for all genotypes with z-axis spacing between 0.2-0.5 µm and optimized for detection without saturation of the signal.

ROS and rotenone incubation assay

Larvae were dissected in ice-cold calcium-free HL3 to label ROS in neurons. ROS levels were detected in mitochondria by incubating live preparation in 1X Schneider's media with MitoSOX™ Red (Molecular Probes, ThermoFisher Scientific) fluorogenic dye at 1:200 dilutions for 20-30

minutes. Briefly, larvae were washed with HL3, mounted in VECTASHIELD (Vector Laboratories, USA.), and immediately imaged in a laser scanning confocal microscope (LSM 710; Carl Zeiss). To study the effect of DMSO and rotenone (Sigma Aldrich) in BRP, larvae were dissected in HL3 and incubated in 1X Schneider's media containing either 500 µM of rotenone or DMSO. After every 30 minutes, the old media was replaced with fresh media containing rotenone or DMSO. The above preparations were fixed with 4% paraformaldehyde, stained with anti-nc82 antibodies, mounted and imaged in a confocal microscope.

Electrophysiology and pharmacology

All dissections and recordings were performed in modified HL-3 saline [112] containing 70 mM NaCl, 5 mM KCl, 10 mM MgCl2, 10 mM NaHCO3, 115 mM sucrose, 4.2 mM trehalose, 5 mM HEPES, and 0.5 mM CaCl2 (unless otherwise noted), pH 7.2. Neuromuscular junction sharp electrode (electrode resistance between 20-30 MΩ) recordings were performed on muscles 6/7 of abdominal segments A2 and A3 in wandering third-instar larvae as described [109]. Recordings were performed on a Leica microscope using a 10x objective and acquired using an Axoclamp 900A amplifier, Digidata 1440A acquisition system, and pClamp 10.7 software (Molecular Devices). Electrophysiological sweeps were digitized at 10 kHz and filtered at 1 kHz. Data were analyzed using Clampfit (Molecular Devices) and MiniAnalysis (Synaptosoft) software. Miniature excitatory postsynaptic potentials (mEPSPs) were recorded in the absence of any stimulation and motor axons were stimulated to elicit excitatory postsynaptic potentials (EPSPs).

Larval crawling assay

Vials containing third instar larvae were analyzed for this assay. Vials were poured with 4 ml of 20% sucrose solution and left for 10 min to let the larvae float on top. Floating third instar animals were poured into a petri dish and washed gently twice with deionized water in a paintbrush. A minimum of 10 larvae of each genotype were analyzed on a 2% agarose gel in a petri dish with gridline markings 1 cm on graph paper. The larvae were acclimatized in the petri dish before videotaping. The average distance crawled (in centimeters) by larvae was calculated based on the average number of gridlines passed in 30 sec [110].

Quantification And Statistical Analysis

973 **Quantification of mitochondrial branch length**

974 Controls and[RNAi] -depleted animals were analyzed using mitochondrial marker Mito-GFP, *D42*
975 driver in cell bodies from larvae ventral nerve cord. All images were processed using image J soft-
976 ware. Z-stacks of individual neurons were merged. The Mito-GFP signal was enhanced by adjusting
977 brightness and contrast. The binary masks were created using Image>Adjust>Threshold., Meth-
978 od:Otsu, and Background:Dark. The branches were generated using Process>Binary>Skeletonised
979 [113]. These skeletonized images were analyzed, and branch length of the individual cluster was
980 manually calculated using image J tools.
981
982 **Imaging quantifications**
983 Maximum intensity projections were used for quantitative image analysis with the Image J software
984 (National Institutes of Health) analysis toolkit. Boutons from muscle 4 or type Ib terminal boutons on
985 the muscle 6/7 of A2 hemisegment from at least six NMJ synapses were used for quantification us-
986 ing Image J software. Student's t-test for pairwise and one-way ANOVA with post-hoc Tukey's test
987 for multiple comparisons was used for statistical analysis, using GraphPad Prism Software. Specific
988 p-value and tests are noted in the figures and figure legends and supplementary files and shown in
989 graphs as follows: *p<0.05, **p<0.001, and ***p<0.0001. The data are presented as mean ± s.e.m.
990 For quantification of Futsch loops, third instar larval preparations were double immunostained with
991 HRP, 22C10 and images were captured in Zeiss LSM710 confocal microscope. Only NMJs of mus-
992 cles 6/7 of A2 hemisegment were used for quantification. The images were digitally magnified using
993 image J software and the total number of HRP-positive boutons was manually counted in each im-
994 age. Futsch positive loops, which are co-localized with HRP, were included in this analysis. Images
995 with incomplete loops and diffused staining were not included in the count [114].
996
997 **Electrophysiological analysis**
998 Average mEPSP, EPSP, and quantal content were calculated for each genotype by dividing EPSP
999 amplitude by mEPSP amplitude. Muscle input resistance (R_{in}) and resting membrane potential
1000 (V_{rest}) were monitored during each experiment. Recordings were rejected if the V_{rest} was above -60
1001 mV, and R_{in} was less than 5 MΩ. Pharmacological agents were bath applied in recording saline at
1002 the final concentrations indicated in the text, figures, and tables. The agents included Xestospongin
1003 C (Abcam), Dantrolene (Tocris) and BAPTA-AM (Sigma Aldrich). Failure analysis was performed in
1004 HL-3 solution containing 0.1 mM CaCl2, which resulted in failures in about half of the stimulated re-
1005 sponses in wild-type larvae. A total of 30 trials (stimulations) were performed at each NMJ in all
1006 genotypes. The failure rate was obtained by dividing the total number of failures by the total number

of trials (100). High-frequency (10 Hz) recordings were performed at a Ca^{2+} concentration of 2 mM and paired-pulse recordings (10 Hz) were performed at a Ca^{2+} concentration of 0.4 mM and 1.5 mM, respectively. Paired-pulse ratios were calculated as the EPSP amplitude of the second response divided by the first response (EPSP2/EPSP1).

REFERENCES

1. Chamberlain, K.A., and Sheng, Z.H. (2019). Mechanisms for the maintenance and regulation of axonal energy supply. Journal of neuroscience research *97*, 897-913. 10.1002/jnr.24411.

2. Hall, C.N., Klein-Flugge, M.C., Howarth, C., and Attwell, D. (2012). Oxidative phosphorylation, not glycolysis, powers presynaptic and postsynaptic mechanisms underlying brain information processing. J Neurosci *32*, 8940-8951. 10.1523/JNEUROSCI.0026-12.2012.

3. Neupane, P., Bhuju, S., Thapa, N., and Bhattarai, H.K. (2019). ATP Synthase: Structure, Function and Inhibition. Biomol Concepts *10*, 1-10. 10.1515/bmc-2019-0001.

4. Brown, G.C. (1992). Control of respiration and ATP synthesis in mammalian mitochondria and cells. Biochem J *284 (Pt 1)*, 1-13. 10.1042/bj2840001.

5. Faria-Pereira, A., and Morais, V.A. (2022). Synapses: The Brain's Energy-Demanding Sites. International journal of molecular sciences *23*. 10.3390/ijms23073627.

6. Vandecasteele, G., Szabadkai, G., and Rizzuto, R. (2001). Mitochondrial calcium homeostasis: mechanisms and molecules. IUBMB Life *52*, 213-219. 10.1080/15216540152846028.

7. Mattson, M.P., Gleichmann, M., and Cheng, A. (2008). Mitochondria in neuroplasticity and neurological disorders. Neuron *60*, 748-766. 10.1016/j.neuron.2008.10.010.

8. Hamanaka, R.B., and Chandel, N.S. (2010). Mitochondrial reactive oxygen species regulate cellular signaling and dictate biological outcomes. Trends Biochem Sci *35*, 505-513. 10.1016/j.tibs.2010.04.002.

9. Kastaniotis, A.J., Autio, K.J., Keratar, J.M., Monteuuis, G., Makela, A.M., Nair, R.R., Pietikainen, L.P., Shvetsova, A., Chen, Z., and Hiltunen, J.K. (2017). Mitochondrial fatty acid synthesis, fatty acids and mitochondrial physiology. Biochim Biophys Acta Mol Cell Biol Lipids *1862*, 39-48. 10.1016/j.bbalip.2016.08.011.

10. Banoth, B., and Cassel, S.L. (2018). Mitochondria in innate immune signaling. Transl Res *202*, 52-68. 10.1016/j.trsl.2018.07.014.

11. Duarte, M., Sousa, R., and Videira, A. (1995). Inactivation of genes encoding subunits of the peripheral and membrane arms of neurospora mitochondrial complex I and effects on enzyme assembly. Genetics *139*, 1211-1221. 10.1093/genetics/139.3.1211.

12. Garcia, C.J., Khajeh, J., Coulanges, E., Chen, E.I., and Owusu-Ansah, E. (2017). Regulation of Mitochondrial Complex I Biogenesis in Drosophila Flight Muscles. Cell reports *20*, 264-278. 10.1016/j.celrep.2017.06.015.

13. Mallik, B., and Frank, C.A. (2022). Roles for Mitochondrial Complex I Subunits in Regulating Synaptic Transmission and Growth. Front Neurosci *16*, 846425. 10.3389/fnins.2022.846425.

14. Sharma, L.K., Lu, J., and Bai, Y. (2009). Mitochondrial respiratory complex I: structure, function and implication in human diseases. Curr Med Chem *16*, 1266-1277. 10.2174/092986709787846578.

15. Yang, J.L., Mukda, S., and Chen, S.D. (2018). Diverse roles of mitochondria in ischemic stroke. Redox Biol *16*, 263-275. 10.1016/j.redox.2018.03.002.

16. Marin, S.E., Mesterman, R., Robinson, B., Rodenburg, R.J., Smeitink, J., and Tarnopolsky, M.A. (2013). Leigh syndrome associated with mitochondrial complex I deficiency due to novel mutations In NDUFV1 and NDUFS2. Gene *516*, 162-167. 10.1016/j.gene.2012.12.024.

17. Goto, Y. (2000). Mitochondrial encephalomyopathy. Neuropathology *20 Suppl*, S82-84. 10.1046/j.1440-1789.2000.00304.x.

18. Shoffner, J.M. (2000). Mitochondrial myopathy diagnosis. Neurol Clin *18*, 105-123. 10.1016/s0733-8619(05)70180-8.

19. Burman, J.L., Itsara, L.S., Kayser, E.B., Suthammarak, W., Wang, A.M., Kaeberlein, M., Sedensky, M.M., Morgan, P.G., and Pallanck, L.J. (2014). A Drosophila model of mitochondrial disease caused by a complex I mutation that uncouples proton pumping from electron transfer. Dis Model Mech *7*, 1165-1174. 10.1242/dmm.015321.

20. Schon, E.A., and Manfredi, G. (2003). Neuronal degeneration and mitochondrial dysfunction. The Journal of clinical investigation *111*, 303-312. 10.1172/JCI17741.

21. He, L., He, T., Farrar, S., Ji, L., Liu, T., and Ma, X. (2017). Antioxidants Maintain Cellular Redox Homeostasis by Elimination of Reactive Oxygen Species. Cell Physiol Biochem *44*, 532-553. 10.1159/000485089.

22. Folbergrova, J., and Kunz, W.S. (2012). Mitochondrial dysfunction in epilepsy. Mitochondrion *12*, 35-40. 10.1016/j.mito.2011.04.004.

23. Lanza, I.R., and Nair, K.S. (2010). Mitochondrial function as a determinant of life span. Pflugers Arch *459*, 277-289. 10.1007/s00424-009-0724-5.

24. Martin, L.J. (2012). Biology of mitochondria in neurodegenerative diseases. Prog Mol Biol Transl Sci *107*, 355-415. 10.1016/B978-0-12-385883-2.00005-9.

25. Pilling, A.D., Horiuchi, D., Lively, C.M., and Saxton, W.M. (2006). Kinesin-1 and Dynein are the primary motors for fast transport of mitochondria in Drosophila motor axons. Molecular biology of the cell *17*, 2057-2068. 10.1091/mbc.E05-06-0526.

26. Misgeld, T., and Schwarz, T.L. (2017). Mitostasis in Neurons: Maintaining Mitochondria in an Extended Cellular Architecture. Neuron *96*, 651-666. 10.1016/j.neuron.2017.09.055.

27. Sheng, Z.H. (2014). Mitochondrial trafficking and anchoring in neurons: New insight and implications. J Cell Biol *204*, 1087-1098. 10.1083/jcb.201312123.

28. Sandoval, H., Yao, C.K., Chen, K., Jaiswal, M., Donti, T., Lin, Y.Q., Bayat, V., Xiong, B., Zhang, K., David, G., et al. (2014). Mitochondrial fusion but not fission regulates larval growth and synaptic development through steroid hormone production. eLife *3*. 10.7554/eLife.03558.

29. Ge, Y., Shi, X., Boopathy, S., McDonald, J., Smith, A.W., and Chao, L.H. (2020). Two forms of Opa1 cooperate to complete fusion of the mitochondrial inner-membrane. eLife *9*. 10.7554/eLife.50973.

30. Song, Z., Ghochani, M., McCaffery, J.M., Frey, T.G., and Chan, D.C. (2009). Mitofusins and OPA1 mediate sequential steps in mitochondrial membrane fusion. Molecular biology of the cell *20*, 3525-3532. 10.1091/mbc.E09-03-0252.

31. Smirnova, E., Griparic, L., Shurland, D.L., and van der Bliek, A.M. (2001). Dynamin-related protein Drp1 is required for mitochondrial division in mammalian cells. Molecular biology of the cell *12*, 2245-2256. 10.1091/mbc.12.8.2245.

32. Twig, G., Elorza, A., Molina, A.J., Mohamed, H., Wikstrom, J.D., Walzer, G., Stiles, L., Haigh, S.E., Katz, S., Las, G., et al. (2008). Fission and selective fusion govern mitochondrial segregation and elimination by autophagy. EMBO J *27*, 433-446. 10.1038/sj.emboj.7601963.

33. Breuer, M.E., Koopman, W.J., Koene, S., Nooteboom, M., Rodenburg, R.J., Willems, P.H., and Smeitink, J.A. (2013). The role of mitochondrial OXPHOS dysfunction in the development of neurologic diseases. Neurobiology of disease *51*, 27-34. 10.1016/j.nbd.2012.03.007.

34. Berger, I., Hershkovitz, E., Shaag, A., Edvardson, S., Saada, A., and Elpeleg, O. (2008). Mitochondrial complex I deficiency caused by a deleterious NDUFA11 mutation. Ann Neurol *63*, 405-408. 10.1002/ana.21332.

35. Formosa, L.E., Muellner-Wong, L., Reljic, B., Sharpe, A.J., Jackson, T.D., Beilharz, T.H., Stojanovski, D., Lazarou, M., Stroud, D.A., and Ryan, M.T. (2020). Dissecting the Roles of Mitochondrial Complex I Intermediate Assembly Complex Factors in the Biogenesis of Complex I. Cell reports *31*, 107541. 10.1016/j.celrep.2020.107541.

36. Guerrero-Castillo, S., Baertling, F., Kownatzki, D., Wessels, H.J., Arnold, S., Brandt, U., and Nijtmans, L. (2017). The Assembly Pathway of Mitochondrial Respiratory Chain Complex I. Cell metabolism *25*, 128-139. 10.1016/j.cmet.2016.09.002.

37. Stroud, D.A., Surgenor, E.E., Formosa, L.E., Reljic, B., Frazier, A.E., Dibley, M.G., Osellame, L.D., Stait, T., Beilharz, T.H., Thorburn, D.R., et al. (2016). Accessory subunits are integral for assembly and function of human mitochondrial complex I. Nature *538*, 123-126. 10.1038/nature19754.

38. Kauffman, M.E., Kauffman, M.K., Traore, K., Zhu, H., Trush, M.A., Jia, Z., and Li, Y.R. (2016). MitoSOX-Based Flow Cytometry for Detecting Mitochondrial ROS. React Oxyg Species (Apex) *2*, 361-370. 10.20455/ros.2016.865.

39. Robinson, K.M., Janes, M.S., Pehar, M., Monette, J.S., Ross, M.F., Hagen, T.M., Murphy, M.P., and Beckman, J.S. (2006). Selective fluorescent imaging of superoxide in vivo using ethidium-based probes. Proc Natl Acad Sci U S A *103*, 15038-15043. 10.1073/pnas.0601945103.

40. Little, A.C., Kovalenko, I., Goo, L.E., Hong, H.S., Kerk, S.A., Yates, J.A., Purohit, V., Lombard, D.B., Merajver, S.D., and Lyssiotis, C.A. (2020). High-content fluorescence imaging with the metabolic flux assay reveals insights into mitochondrial properties and functions. Commun Biol *3*, 271. 10.1038/s42003-020-0988-z.

41. Martelli, F., Hernandes, N.H., Zuo, Z., Wang, J., Wong, C.O., Karagas, N.E., Roessner, U., Rupasinghe, T., Robin, C., Venkatachalam, K., et al. (2022). Low doses of the organic insecticide spinosad trigger lysosomal defects, elevated ROS, lipid dysregulation, and neurodegeneration in flies. eLife *11*. 10.7554/eLife.73812.

42. Martelli, F., Zhongyuan, Z., Wang, J., Wong, C.O., Karagas, N.E., Roessner, U., Rupasinghe, T., Venkatachalam, K., Perry, T., Bellen, H.J., and Batterham, P. (2020). Low doses of the neonicotinoid insecticide imidacloprid induce ROS triggering neurological and metabolic impairments in Drosophila. Proc Natl Acad Sci U S A *117*, 25840-25850. 10.1073/pnas.2011828117.

43. Penugonda, S., Mare, S., Lutz, P., Banks, W.A., and Ercal, N. (2006). Potentiation of lead-induced cell death in PC12 cells by glutamate: protection by N-acetylcysteine amide (NACA), a novel thiol antioxidant. Toxicol Appl Pharmacol *216*, 197-205. 10.1016/j.taap.2006.05.002.

44. Missirlis, F., Hu, J., Kirby, K., Hilliker, A.J., Rouault, T.A., and Phillips, J.P. (2003). Compartment-specific protection of iron-sulfur proteins by superoxide dismutase. J Biol Chem *278*, 47365-47369. 10.1074/jbc.M307700200.

45. Oswald, M.C.W., Garnham, N., Sweeney, S.T., and Landgraf, M. (2018). Regulation of neuronal development and function by ROS. FEBS letters *592*, 679-691. 10.1002/1873-3468.12972.

46. Roos, J., Hummel, T., Ng, N., Klambt, C., and Davis, G.W. (2000). Drosophila Futsch regulates synaptic microtubule organization and is necessary for synaptic growth. Neuron *26*, 371-382.

47. Guo, X., Macleod, G.T., Wellington, A., Hu, F., Panchumarthi, S., Schoenfield, M., Marin, L., Charlton, M.P., Atwood, H.L., and Zinsmaier, K.E. (2005). The GTPase dMiro is required for axonal transport of mitochondria to Drosophila synapses. Neuron *47*, 379-393. 10.1016/j.neuron.2005.06.027.

48. Verstreken, P., Ly, C.V., Venken, K.J., Koh, T.W., Zhou, Y., and Bellen, H.J. (2005). Synaptic mitochondria are critical for mobilization of reserve pool vesicles at Drosophila neuromuscular junctions. Neuron *47*, 365-378. 10.1016/j.neuron.2005.06.018.

49. Milton, V.J., Jarrett, H.E., Gowers, K., Chalak, S., Briggs, L., Robinson, I.M., and Sweeney, S.T. (2011). Oxidative stress induces overgrowth of the Drosophila neuromuscular junction. Proc Natl Acad Sci U S A *108*, 17521-17526. 10.1073/pnas.1014511108.

50. Oswald, M.C., Brooks, P.S., Zwart, M.F., Mukherjee, A., West, R.J., Giachello, C.N., Morarach, K., Baines, R.A., Sweeney, S.T., and Landgraf, M. (2018). Reactive oxygen species regulate activity-dependent neuronal plasticity in Drosophila. eLife *7*. 10.7554/eLife.39393.

51. Böhme, M.A., McCarthy, A.W., Grasskamp, A.T., Beuschel, C.B., Goel, P., Jusyte, M., Laber, D., Huang, S., Rey, U., Petzoldt, A.G., et al. (2019). Rapid active zone remodeling consolidates presynaptic potentiation. Nat Commun *10*, 1085. 10.1038/s41467-019-08977-6.

52. Goel, P., Dufour Bergeron, D., Bohme, M.A., Nunnelly, L., Lehmann, M., Buser, C., Walter, A.M., Sigrist, S.J., and Dickman, D. (2019). Homeostatic scaling of active zone scaffolds maintains global synaptic strength. J Cell Biol *218*, 1706-1724. 10.1083/jcb.201807165.

53. Gratz, S.J., Goel, P., Bruckner, J.J., Hernandez, R.X., Khateeb, K., Macleod, G.T., Dickman, D., and O'Connor-Giles, K.M. (2019). Endogenous Tagging Reveals Differential Regulation of Ca(2+) Channels at Single Active Zones during Presynaptic Homeostatic Potentiation and Depression. J Neurosci *39*, 2416-2429. 10.1523/JNEUROSCI.3068-18.2019.

54. Hong, H., Zhao, K., Huang, S., Huang, S., Yao, A., Jiang, Y., Sigrist, S., Zhao, L., and Zhang, Y.Q. (2020). Structural Remodeling of Active Zones Is Associated with Synaptic Homeostasis. J Neurosci *40*, 2817-2827. 10.1523/JNEUROSCI.2002-19.2020.

55. Dannhauser, S., Mrestani, A., Gundelach, F., Pauli, M., Komma, F., Kollmannsberger, P., Sauer, M., Heckmann, M., and Paul, M.M. (2022). Endogenous tagging of Unc-13 reveals nanoscale reorganization at active zones during presynaptic homeostatic potentiation. Frontiers in cellular neuroscience *16*, 1074304. 10.3389/fncel.2022.1074304.

56. Ashrafi, G., de Juan-Sanz, J., Farrell, R.J., and Ryan, T.A. (2020). Molecular Tuning of the Axonal Mitochondrial Ca(2+) Uniporter Ensures Metabolic Flexibility of Neurotransmission. Neuron *105*, 678-687 e675. 10.1016/j.neuron.2019.11.020.

57. Datta, S., and Jaiswal, M. (2021). Mitochondrial calcium at the synapse. Mitochondrion *59*, 135-153. 10.1016/j.mito.2021.04.006.

58. Marland, J.R., Hasel, P., Bonnycastle, K., and Cousin, M.A. (2016). Mitochondrial Calcium Uptake Modulates Synaptic Vesicle Endocytosis in Central Nerve Terminals. J Biol Chem *291*, 2080-2086. 10.1074/jbc.M115.686956.

59. Paradis, M., Kucharowski, N., Edwards Faret, G., Maya Palacios, S.J., Meyer, C., Stumpges, B., Jamitzky, I., Kalinowski, J., Thiele, C., Bauer, R., et al. (2022). The ER protein Creld regulates ER-mitochondria contact dynamics and respiratory complex 1 activity. Sci Adv *8*, eabo0155. 10.1126/sciadv.abo0155.

60. Benson, T.E., and Voigt, H.F. (1995). Neuron labeling by extracellular delivery of horseradish peroxidase in vivo: a method for studying the local circuitry of projection and

interneurons at physiologically characterized sites. J Neurosci Methods *57*, 81-91. 10.1016/0165-0270(94)00131-y.

61. Budnik, V., Koh, Y.H., Guan, B., Hartmann, B., Hough, C., Woods, D., and Gorczyca, M. (1996). Regulation of synapse structure and function by the Drosophila tumor suppressor gene dlg. Neuron *17*, 627-640.

62. Pielage, J., Fetter, R.D., and Davis, G.W. (2006). A postsynaptic spectrin scaffold defines active zone size, spacing, and efficacy at the Drosophila neuromuscular junction. J Cell Biol *175*, 491-503.

63. Chen, K., and Featherstone, D.E. (2005). Discs-large (DLG) is clustered by presynaptic innervation and regulates postsynaptic glutamate receptor subunit composition in Drosophila. BMC Biol *3*, 1. 10.1186/1741-7007-3-1.

64. Accardi, M.V., Daniels, B.A., Brown, P.M., Fritschy, J.M., Tyagarajan, S.K., and Bowie, D. (2014). Mitochondrial reactive oxygen species regulate the strength of inhibitory GABA-mediated synaptic transmission. Nat Commun *5*, 3168. 10.1038/ncomms4168.

65. Doser, R.L., Amberg, G.C., and Hoerndli, F.J. (2020). Reactive Oxygen Species Modulate Activity-Dependent AMPA Receptor Transport in C. elegans. J Neurosci *40*, 7405-7420. 10.1523/JNEUROSCI.0902-20.2020.

66. Peng, J.J., Lin, S.H., Liu, Y.T., Lin, H.C., Li, T.N., and Yao, C.K. (2019). A circuit-dependent ROS feedback loop mediates glutamate excitotoxicity to sculpt the Drosophila motor system. eLife *8*. 10.7554/eLife.47372.

67. Wang, X., Winter, D., Ashrafi, G., Schlehe, J., Wong, Y.L., Selkoe, D., Rice, S., Steen, J., LaVoie, M.J., and Schwarz, T.L. (2011). PINK1 and Parkin target Miro for phosphorylation and degradation to arrest mitochondrial motility. Cell *147*, 893-906. 10.1016/j.cell.2011.10.018.

68. Wang, X., and Schwarz, T.L. (2009). The mechanism of Ca2+ -dependent regulation of kinesin-mediated mitochondrial motility. Cell *136*, 163-174. 10.1016/j.cell.2008.11.046.

69. Clark, I.E., Dodson, M.W., Jiang, C., Cao, J.H., Huh, J.R., Seol, J.H., Yoo, S.J., Hay, B.A., and Guo, M. (2006). Drosophila pink1 is required for mitochondrial function and interacts genetically with parkin. Nature *441*, 1162-1166. 10.1038/nature04779.

70. Park, J., Lee, S.B., Lee, S., Kim, Y., Song, S., Kim, S., Bae, E., Kim, J., Shong, M., Kim, J.M., and Chung, J. (2006). Mitochondrial dysfunction in Drosophila PINK1 mutants is complemented by parkin. Nature *441*, 1157-1161. 10.1038/nature04788.

71. Poole, A.C., Thomas, R.E., Andrews, L.A., McBride, H.M., Whitworth, A.J., and Pallanck, L.J. (2008). The PINK1/Parkin pathway regulates mitochondrial morphology. Proc Natl Acad Sci U S A *105*, 1638-1643. 10.1073/pnas.0709336105.

72. Yang, Y., Gehrke, S., Imai, Y., Huang, Z., Ouyang, Y., Wang, J.W., Yang, L., Beal, M.F., Vogel, H., and Lu, B. (2006). Mitochondrial pathology and muscle and dopaminergic neuron degeneration caused by inactivation of Drosophila Pink1 is rescued by Parkin. Proc Natl Acad Sci U S A *103*, 10793-10798. 10.1073/pnas.0602493103.

73. Jiang, H.C., Hsu, J.M., Yen, C.P., Chao, C.C., Chen, R.H., and Pan, C.L. (2015). Neural activity and CaMKII protect mitochondria from fragmentation in aging Caenorhabditis elegans neurons. Proc Natl Acad Sci U S A *112*, 8768-8773. 10.1073/pnas.1501831112.

74. Obashi, K., and Okabe, S. (2013). Regulation of mitochondrial dynamics and distribution by synapse position and neuronal activity in the axon. The European journal of neuroscience *38*, 2350-2363. 10.1111/ejn.12263.

75. Lin, M.T., and Beal, M.F. (2006). Mitochondrial dysfunction and oxidative stress in neurodegenerative diseases. Nature *443*, 787-795. 10.1038/nature05292.

76. Esterberg, R., Linbo, T., Pickett, S.B., Wu, P., Ou, H.C., Rubel, E.W., and Raible, D.W. (2016). Mitochondrial calcium uptake underlies ROS generation during aminoglycoside-induced hair cell death. The Journal of clinical investigation *126*, 3556-3566. 10.1172/JCI84939.

77. Gorlach, A., Bertram, K., Hudecova, S., and Krizanova, O. (2015). Calcium and ROS: A mutual interplay. Redox Biol *6*, 260-271. 10.1016/j.redox.2015.08.010.

78. Yu, T., Robotham, J.L., and Yoon, Y. (2006). Increased production of reactive oxygen species in hyperglycemic conditions requires dynamic change of mitochondrial morphology. Proc Natl Acad Sci U S A *103*, 2653-2658. 10.1073/pnas.0511154103.

79. Jornayvaz, F.R., and Shulman, G.I. (2010). Regulation of mitochondrial biogenesis. Essays Biochem *47*, 69-84. 10.1042/bse0470069.

80. Shaw, J.M., and Winge, D.R. (2009). Shaping the mitochondrion: mitochondrial biogenesis, dynamics and dysfunction. Conference on Mitochondrial Assembly and Dynamics in Health and Disease. EMBO reports *10*, 1301-1305. 10.1038/embor.2009.247.

81. Esparza-Molto, P.B., Romero-Carraminana, I., Nunez de Arenas, C., Pereira, M.P., Blanco, N., Pardo, B., Bates, G.R., Sanchez-Castillo, C., Artuch, R., Murphy, M.P., et al. (2021). Generation of mitochondrial reactive oxygen species is controlled by ATPase inhibitory factor 1 and regulates cognition. PLoS Biol *19*, e3001252. 10.1371/journal.pbio.3001252.

82. Huddleston, A.T., Tang, W., Takeshima, H., Hamilton, S.L., and Klann, E. (2008). Superoxide-induced potentiation in the hippocampus requires activation of ryanodine receptor type 3 and ERK. Journal of neurophysiology *99*, 1565-1571. 10.1152/jn.00659.2007.

83. Lee, K.Y., Chung, K., and Chung, J.M. (2010). Involvement of reactive oxygen species in long-term potentiation in the spinal cord dorsal horn. Journal of neurophysiology *103*, 382-391. 10.1152/jn.90906.2008.

84. Müller, M., Pym, E.C., Tong, A., and Davis, G.W. (2011). Rab3-GAP controls the progression of synaptic homeostasis at a late stage of vesicle release. Neuron *69*, 749-762. S0896-6273(11)00073-0 [pii]

10.1016/j.neuron.2011.01.025.

85. Frank, C.A., Kennedy, M.J., Goold, C.P., Marek, K.W., and Davis, G.W. (2006). Mechanisms underlying the rapid induction and sustained expression of synaptic homeostasis. Neuron *52*, 663-677.

86. Petersen, S.A., Fetter, R.D., Noordermeer, J.N., Goodman, C.S., and DiAntonio, A. (1997). Genetic analysis of glutamate receptors in Drosophila reveals a retrograde signal regulating presynaptic transmitter release. Neuron *19*, 1237-1248.

87. Frank, C.A., Pielage, J., and Davis, G.W. (2009). A presynaptic homeostatic signaling system composed of the Eph receptor, ephexin, Cdc42, and CaV2.1 calcium channels. Neuron *61*, 556-569.

88. Müller, M., and Davis, G.W. (2012). Transsynaptic control of presynaptic Ca(2)(+) influx achieves homeostatic potentiation of neurotransmitter release. Curr Biol *22*, 1102-1108. 10.1016/j.cub.2012.04.018

S0960-9822(12)00410-1 [pii].

89. Wang, T., Hauswirth, A.G., Tong, A., Dickman, D.K., and Davis, G.W. (2014). Endostatin Is a Trans-Synaptic Signal for Homeostatic Synaptic Plasticity. Neuron *83*, 616-629. 10.1016/j.neuron.2014.07.003.

90. Younger, M.A., Müller, M., Tong, A., Pym, E.C., and Davis, G.W. (2013). A presynaptic ENaC channel drives homeostatic plasticity. Neuron *79*, 1183-1196. 10.1016/j.neuron.2013.06.048.

91. Harris, N., Braiser, D.J., Dickman, D.K., Fetter, R.D., Tong, A., and Davis, G.W. (2015). The Innate Immune Receptor PGRP-LC Controls Presynaptic Homeostatic Plasticity. Neuron *88*, 1157-1164. 10.1016/j.neuron.2015.10.049.

92. Müller, M., Genç, Ö., and Davis, G.W. (2015). RIM-Binding Protein Links Synaptic Homeostasis to the Stabilization and Replenishment of High Release Probability Vesicles. Neuron *85*, 1056-1069. 10.1016/j.neuron.2015.01.024.

93. Müller, M., Liu, K.S., Sigrist, S.J., and Davis, G.W. (2012). RIM Controls Homeostatic Plasticity through Modulation of the Readily-Releasable Vesicle Pool. J Neurosci *32*, 16574-16585. 10.1523/JNEUROSCI.0981-12.2012

32/47/16574 [pii].

94. Weyhersmüller, A., Hallermann, S., Wagner, N., and Eilers, J. (2011). Rapid active zone remodeling during synaptic plasticity. J Neurosci *31*, 6041-6052. 31/16/6041 [pii]

10.1523/JNEUROSCI.6698-10.2011.

95. Goel, P., Dufour Bergeron, D., Bohme, M.A., Nunnelly, L., Lehmann, M., Buser, C., Walter, A.M., Sigrist, S.J., and Dickman, D. (2019). Homeostatic scaling of active zone scaffolds maintains global synaptic strength. J Cell Biol. 10.1083/jcb.201807165.

96. Dhawan, S., Myers, P., Bailey, D.M.D., Ostrovsky, A.D., Evers, J.F., and Landgraf, M. (2021). Reactive Oxygen Species Mediate Activity-Regulated Dendritic Plasticity Through

NADPH Oxidase and Aquaporin Regulation. Frontiers in cellular neuroscience *15*, 641802. 10.3389/fncel.2021.641802.

97. Frank, C.A., James, T.D., and Müller, M. (2020). Homeostatic control of Drosophila neuromuscular junction function. Synapse *74*, e22133. 10.1002/syn.22133.

98. Goold, C.P., and Davis, G.W. (2007). The BMP ligand Gbb gates the expression of synaptic homeostasis independent of synaptic growth control. Neuron *56*, 109-123.

99. Haghighi, A.P., McCabe, B.D., Fetter, R.D., Palmer, J.E., Hom, S., and Goodman, C.S. (2003). Retrograde control of synaptic transmission by postsynaptic CaMKII at the Drosophila neuromuscular junction. Neuron *39*, 255-267.

100. McCabe, B.D., Marques, G., Haghighi, A.P., Fetter, R.D., Crotty, M.L., Haerry, T.E., Goodman, C.S., and O'Connor, M.B. (2003). The BMP homolog Gbb provides a retrograde signal that regulates synaptic growth at the Drosophila neuromuscular junction. Neuron *39*, 241-254.

101. Kikuma, K., Li, X., Perry, S., Li, Q., Goel, P., Chen, C., Kim, D., Stavropoulos, N., and Dickman, D. (2019). Cul3 and insomniac are required for rapid ubiquitination of postsynaptic targets and retrograde homeostatic signaling. Nat Commun *10*, 2998. 10.1038/s41467-019-10992-6.

102. Hauswirth, A.G., Ford, K.J., Wang, T., Fetter, R.D., Tong, A., and Davis, G.W. (2018). A postsynaptic PI3K-cII dependent signaling controller for presynaptic homeostatic plasticity. eLife *7*. 10.7554/eLife.31535.

103. Orr, B.O., Fetter, R.D., and Davis, G.W. (2017). Retrograde semaphorin-plexin signalling drives homeostatic synaptic plasticity. Nature *550*, 109-113. 10.1038/nature24017.

104. Goel, P., Li, X., and Dickman, D. (2017). Disparate Postsynaptic Induction Mechanisms Ultimately Converge to Drive the Retrograde Enhancement of Presynaptic Efficacy. Cell reports *21*, 2339-2347. 10.1016/j.celrep.2017.10.116.

105. Penney, J., Tsurudome, K., Liao, E.H., Elazzouzi, F., Livingstone, M., Gonzalez, M., Sonenberg, N., and Haghighi, A.P. (2012). TOR is required for the retrograde regulation of synaptic homeostasis at the Drosophila neuromuscular junction. Neuron *74*, 166-178. S0896-6273(12)00186-9 [pii]

10.1016/j.neuron.2012.01.030.

106. Pielage, J., Fetter, R.D., and Davis, G.W. (2005). Presynaptic spectrin is essential for synapse stabilization. Curr Biol *15*, 918-928.

107. Pielage, J., Cheng, L., Fetter, R.D., Carlton, P.M., Sedat, J.W., and Davis, G.W. (2008). A presynaptic giant ankyrin stabilizes the NMJ through regulation of presynaptic microtubules and transsynaptic cell adhesion. Neuron *58*, 195-209. 10.1016/j.neuron.2008.02.017.

108. Stephan, R., Goellner, B., Moreno, E., Frank, C.A., Hugenschmidt, T., Genoud, C., Aberle, H., and Pielage, J. (2015). Hierarchical microtubule organization controls axon caliber and transport and determines synaptic structure and stability. Dev Cell *33*, 5-21. 10.1016/j.devcel.2015.02.003.

109. James, T.D., Zwiefelhofer, D.J., and Frank, C.A. (2019). Maintenance of homeostatic plasticity at the Drosophila neuromuscular synapse requires continuous IP3-directed signaling. eLife *8*. 10.7554/eLife.39643.

110. Raut, S., Mallik, B., Parichha, A., Amrutha, V., Sahi, C., and Kumar, V. (2017). RNAi-Mediated Reverse Genetic Screen Identified Drosophila Chaperones Regulating Eye and Neuromuscular Junction Morphology. G3 (Bethesda) *7*, 2023-2038. 10.1534/g3.117.041632.

111. Marrus, S.B., Portman, S.L., Allen, M.J., Moffat, K.G., and DiAntonio, A. (2004). Differential localization of glutamate receptor subunits at the Drosophila neuromuscular junction. J Neurosci *24*, 1406-1415.

112. Stewart, B.A., Atwood, H.L., Renger, J.J., Wang, J., and Wu, C.F. (1994). Improved stability of Drosophila larval neuromuscular preparations in haemolymph-like physiological solutions. J Comp Physiol A *175*, 179-191. 10.1007/BF00215114.

113. Terriente-Felix, A., Wilson, E.L., and Whitworth, A.J. (2020). Drosophila phosphatidylinositol-4 kinase fwd promotes mitochondrial fission and can suppress Pink1/parkin phenotypes. PLoS genetics *16*, e1008844. 10.1371/journal.pgen.1008844.

114. Choudhury, S.D., Mushtaq, Z., Reddy-Alla, S., Balakrishnan, S.S., Thakur, R.S., Krishnan, K.S., Raghu, P., Ramaswami, M., and Kumar, V. (2016). sigma2-Adaptin Facilitates Basal Synaptic Transmission and Is Required for Regenerating Endo-Exo Cycling Pool Under High-Frequency Nerve Stimulation in Drosophila. Genetics *203*, 369-385. 10.1534/genetics.115.183863.

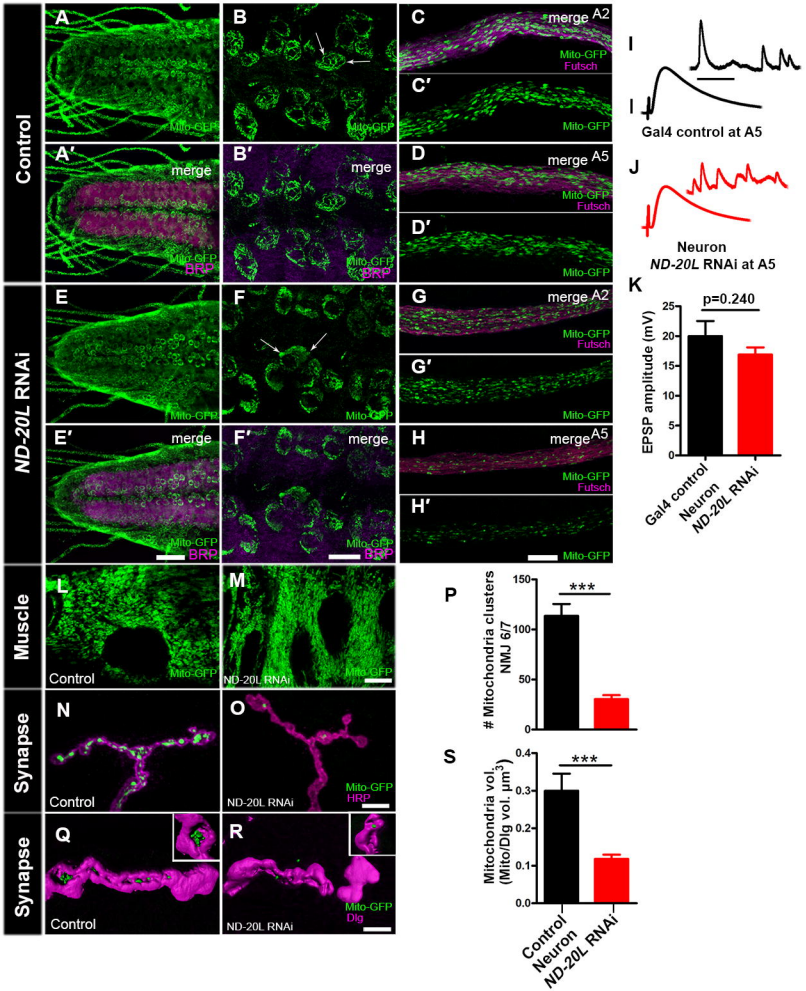
Control
ND-20L RNAi
Muscle
Synapse
Synapse
A
B
C
merge A2
Mito-GFP
Futsch
C′
Mito-GFP
A′
merge
Mito-GFP
BRP
B′
merge
Mito-GFP
BRP
D
merge A5
Mito-GFP
Futsch
D′
Mito-GFP
E
Mito-GFP
F
Mito-GFP
G
merge A2
Mito-GFP
Futsch
G′
Mito-GFP
E′
merge
Mito-GFP
BRP
F′
merge
Mito-GFP
BRP
H
merge A5
Mito-GFP
Futsch
H′
Mito-GFP
L
Control
Mito-GFP
M
ND-20L RNAi
Mito-GFP
N
Control
O
ND-20L RNAi
Mito-GFP
HRP
Q
Control
R
ND-20L RNAi
Mito-GFP
Dlg
I
I
Gal4 control at A5
J
Neuron
ND-20L RNAi at A5
K
p=0.240
EPSP amplitude (mV)
25
20
15
10
5
0
Gal4 control
Neuron
ND-20L RNAi
P
Mitochondria clusters
NMJ 6/7
150
100
50
0
***
S
Mitochondria vol.
(Mito/Dlg vol. μm3)
0.4
0.3
0.2
0.1
0.0
***
Control
Neuron
ND-20L RNAi

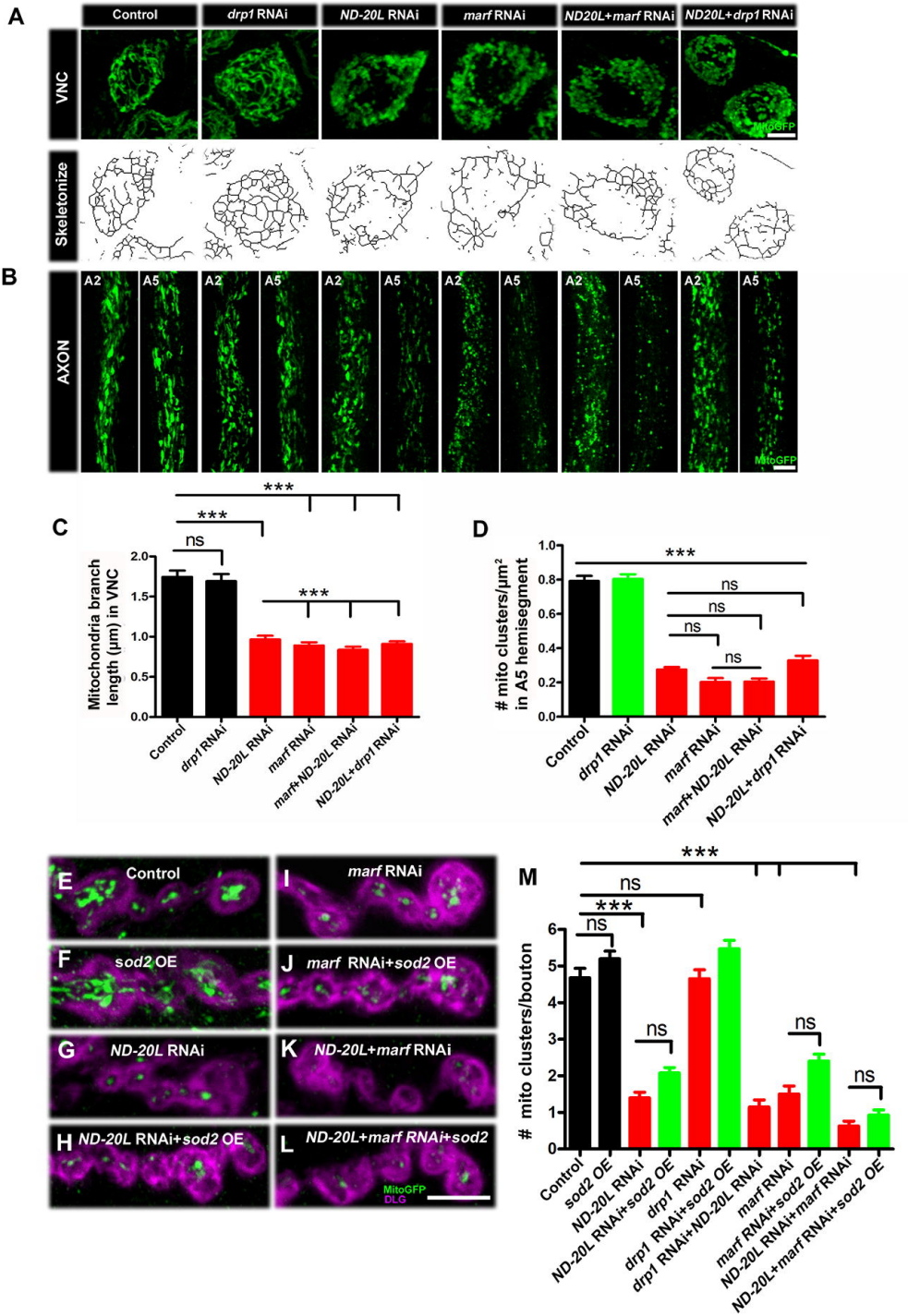
A
Control
drp1 RNAi
ND-20L RNAi
marf RNAi
ND20L+marf RNAi
ND20L+drp1 RNAi
VNC
MitoGFP
Skeletonize
B
AXON
A2
A5
MitoGFP
C
Mitochondria branch length (μm) in VNC
ns
***
***
***
Control
drp1 RNAi
ND-20L RNAi
marf RNAi
marf+ND-20L RNAi
ND-20L+drp1 RNAi
D
mito clusters/μm² in A5 hemisegment
***
ns
ns
ns
ns
Control
drp1 RNAi
ND-20L RNAi
marf RNAi
marf+ND-20L RNAi
ND-20L+drp1 RNAi
E Control
F sod2 OE
G ND-20L RNAi
H ND-20L RNAi+sod2 OE
I marf RNAi
J marf RNAi+sod2 OE
K ND-20L+marf RNAi
L ND-20L+marf RNAi+sod2
MitoGFP
DLG
M
mito clusters/bouton
***
ns
***
ns
ns
ns
ns
Control
sod2 OE
ND-20L RNAi
ND-20L RNAi+sod2 OE
drp1 RNAi
drp1 RNAi+sod2 OE
drp1 RNAi+ND-20L RNAi
marf RNAi
marf RNAi+sod2 OE
ND-20L RNAi+marf RNAi
ND-20L+marf RNAi+sod2 OE

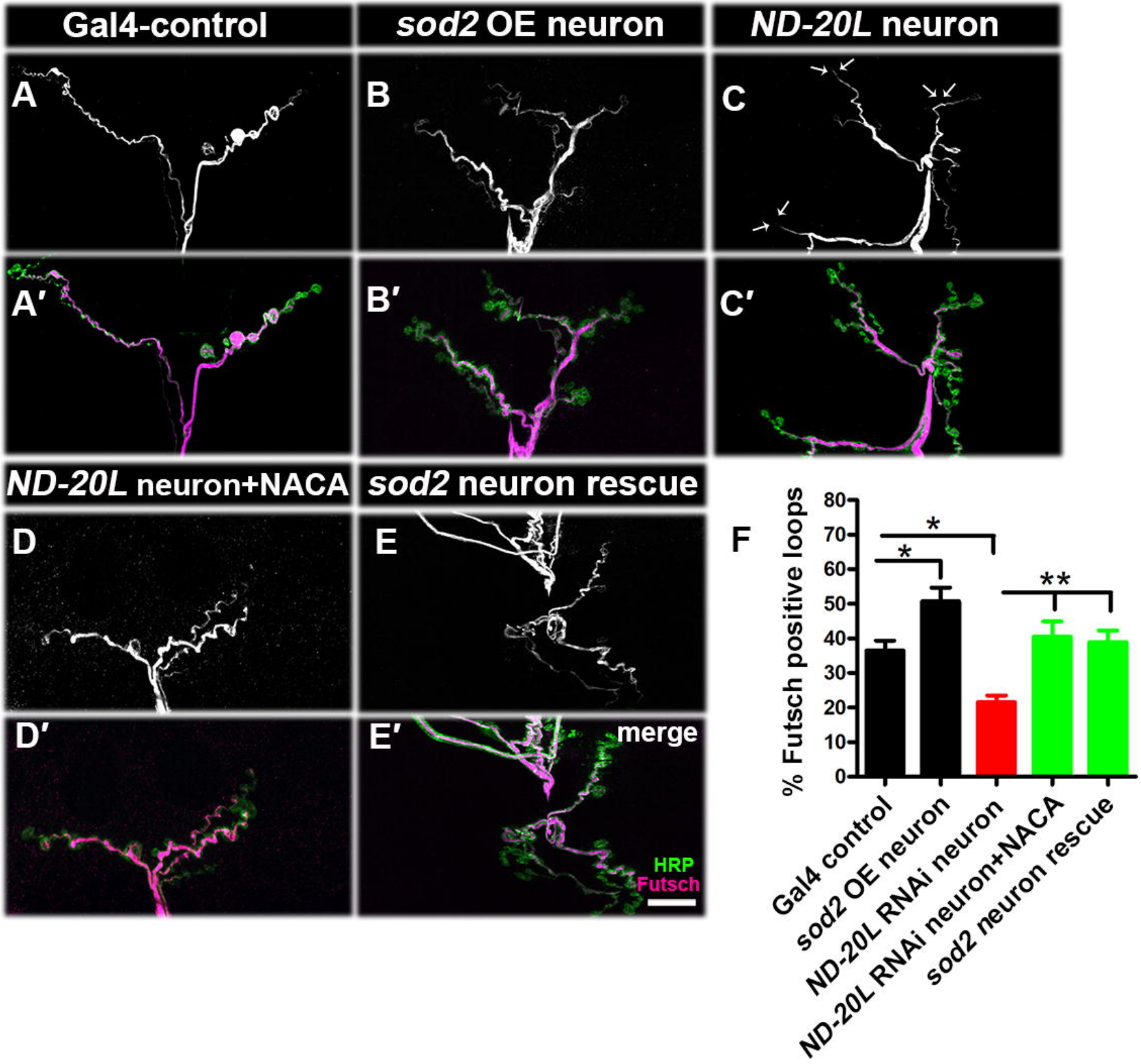
Gal4-control
sod2 OE neuron
ND-20L neuron
A
B
C
A′
B′
C′
ND-20L neuron+NACA
sod2 neuron rescue
D
E
D′
E′
merge
HRP
Futsch
F
% Futsch positive loops
80
70
60
50
40
30
20
10
0
*
*
**
Gal4 control
sod2 OE neuron
ND-20L RNAi neuron
ND-20L RNAi neuron+NACA
sod2 neuron rescue

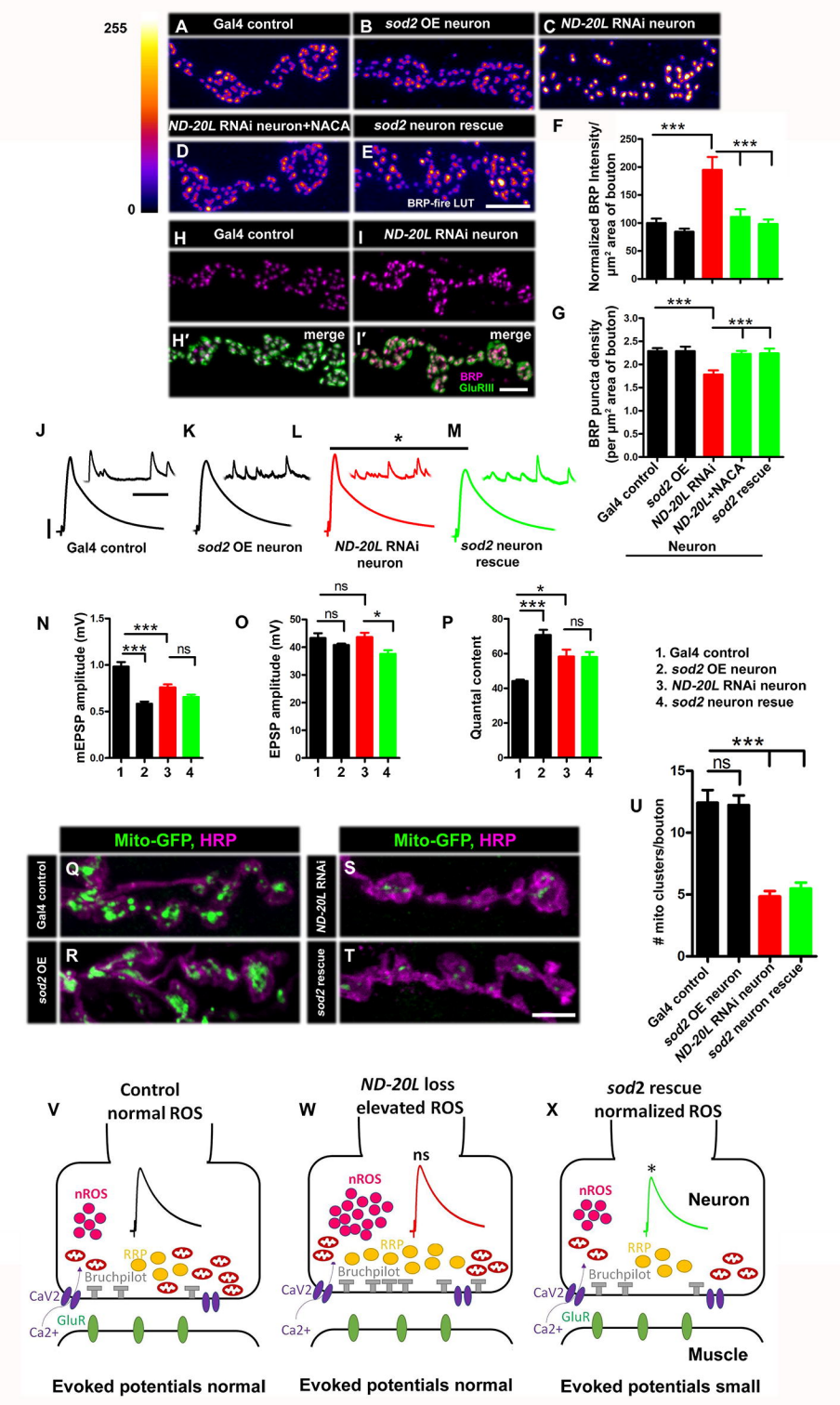
255
0
A Gal4 control
B sod2 OE neuron
C ND-20L RNAi neuron
ND-20L RNAi neuron+NACA
sod2 neuron rescue
D
E
BRP-fire LUT
H Gal4 control
I ND-20L RNAi neuron
H′ merge
I′ merge
BRP
GluRIII
F
Normalized BRP Intensity/ µm² area of bouton
***
***
G
BRP puncta density (per µm² area of bouton)
***
***
Gal4 control
sod2 OE
ND-20L RNAi
ND-20L+NACA
sod2 rescue
Neuron
J
K
L
M
*
Gal4 control
sod2 OE neuron
ND-20L RNAi neuron
sod2 neuron rescue
N
mEPSP amplitude (mV)
***
***
ns
O
EPSP amplitude (mV)
ns
ns
*
P
Quantal content
*
***
ns
1 2 3 4
1. Gal4 control
2. sod2 OE neuron
3. ND-20L RNAi neuron
4. sod2 neuron resue
U
mito clusters/bouton
***
ns
Gal4 control
sod2 OE neuron
ND-20L RNAi neuron
sod2 neuron rescue
Mito-GFP, HRP
Mito-GFP, HRP
Gal4 control
sod2 OE
ND-20L RNAi
sod2 rescue
Q
R
S
T
V Control normal ROS
W ND-20L loss elevated ROS
X sod2 rescue normalized ROS
nROS
RRP
Bruchpilot
CaV2
GluR
Ca2+
ns
*
Neuron
Muscle
Evoked potentials normal
Evoked potentials normal
Evoked potentials small

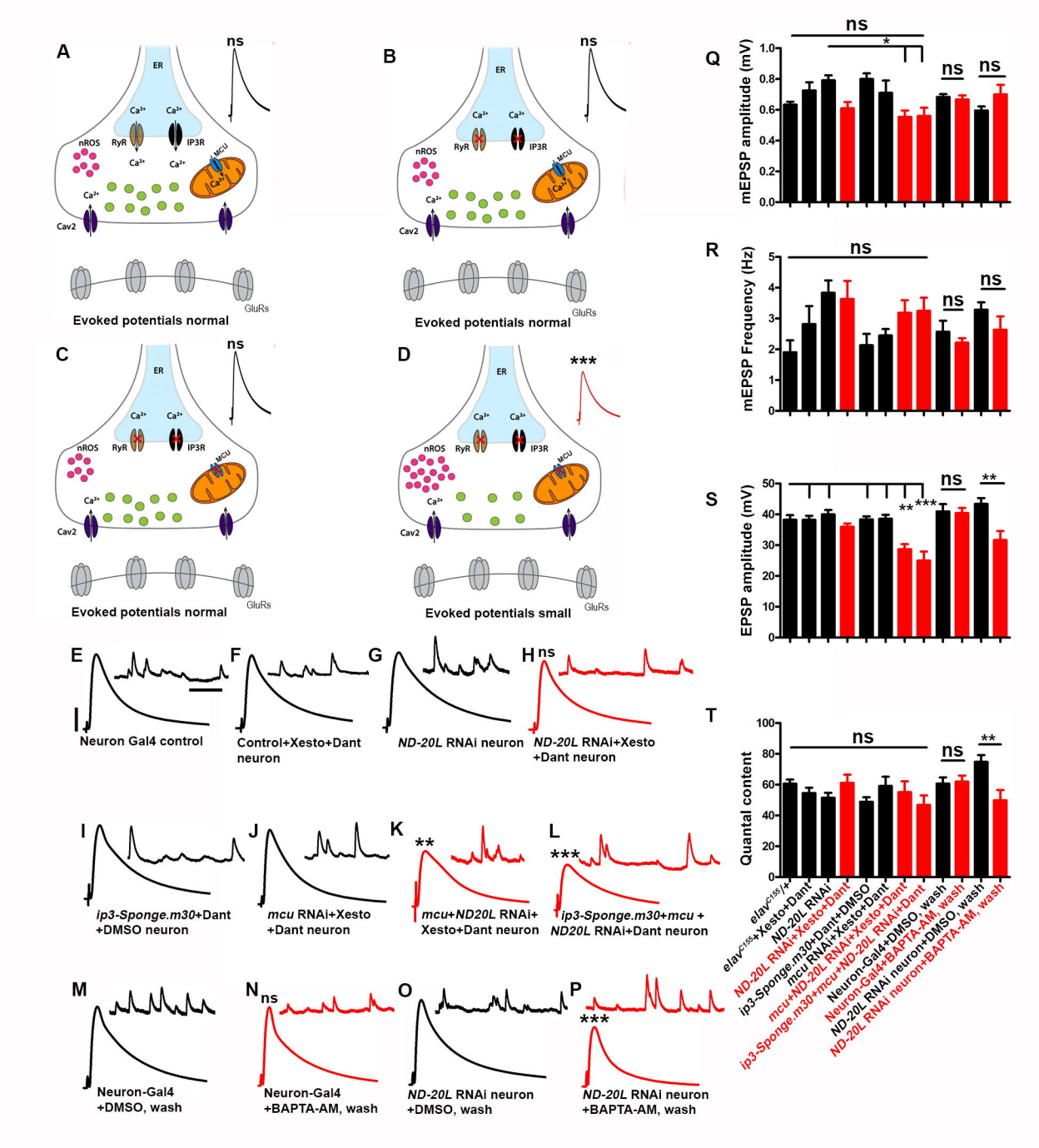
A
ns
ER
Ca2+
RyR
IP3R
nROS
MCU
Cav2
GluRs
Evoked potentials normal
B
ns
Evoked potentials normal
C
ns
Evoked potentials normal
D
***
Evoked potentials small
E
Neuron Gal4 control
F
Control+Xesto+Dant neuron
G
ND-20L RNAi neuron
H
ns
ND-20L RNAi+Xesto +Dant neuron
I
ip3-Sponge.m30+Dant +DMSO neuron
J
mcu RNAi+Xesto +Dant neuron
K
**
mcu+ND20L RNAi+ Xesto+Dant neuron
L
***
ip3-Sponge.m30+mcu + ND20L RNAi+Dant neuron
M
Neuron-Gal4 +DMSO, wash
N
ns
Neuron-Gal4 +BAPTA-AM, wash
O
ND-20L RNAi neuron +DMSO, wash
P
***
ND-20L RNAi neuron +BAPTA-AM, wash
Q
mEPSP amplitude (mV)
ns
*
R
mEPSP Frequency (Hz)
S
EPSP amplitude (mV)
**
T
Quantal content
elavC155/+
elavC155/+Xesto+Dant
ND-20L RNAi
ND-20L RNAi+DMSO
ip3-Sponge.m30+Dant+DMSO
mcu RNAi+Xesto+Dant
ND-20L RNAi+Xesto+Dant
mcu+ND-20L RNAi+Xesto+Dant
ip3-Sponge.m30+mcu+ND-20L RNAi+Dant
Neuron-Gal4+DMSO, wash
Neuron-Gal4+BAPTA-AM, wash
ND-20L RNAi neuron+DMSO, wash
ND-20L RNAi neuron+BAPTA-AM, wash

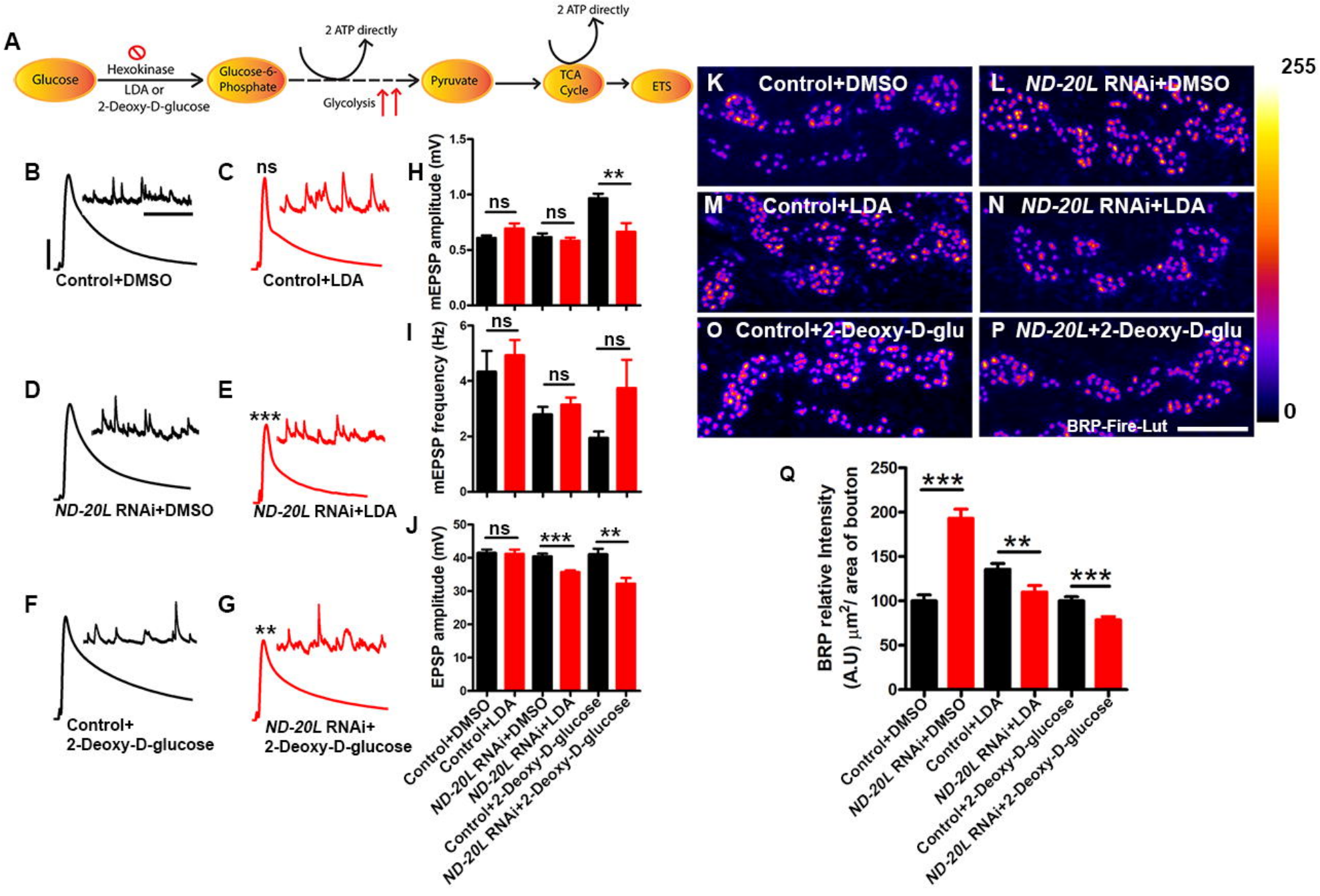
A
Glucose
Hexokinase
LDA or
2-Deoxy-D-glucose
Glucose-6-Phosphate
2 ATP directly
Glycolysis
Pyruvate
2 ATP directly
TCA Cycle
ETS
B
Control+DMSO
C
ns
Control+LDA
D
ND-20L RNAi+DMSO
E
***
ND-20L RNAi+LDA
F
Control+
2-Deoxy-D-glucose
G
**
ND-20L RNAi+
2-Deoxy-D-glucose
H
mEPSP amplitude (mV)
1.5
1.0
0.5
0.0
ns
ns
**
I
mEPSP frequency (Hz)
6
4
2
0
ns
ns
ns
J
EPSP amplitude (mV)
50
40
30
20
10
0
ns
***
**
Control+DMSO
Control+LDA
ND-20L RNAi+DMSO
ND-20L RNAi+LDA
Control+2-Deoxy-D-glucose
ND-20L RNAi+2-Deoxy-D-glucose
K Control+DMSO
L ND-20L RNAi+DMSO
M Control+LDA
N ND-20L RNAi+LDA
O Control+2-Deoxy-D-glu
P ND-20L+2-Deoxy-D-glu
BRP-Fire-Lut
255
0
Q
BRP relative Intensity
(A.U) μm2/ area of bouton
250
200
150
100
50
0
***
**
***
Control+DMSO
ND-20L RNAi+DMSO
Control+LDA
ND-20L RNAi+LDA
Control+2-Deoxy-D-glucose
ND-20L RNAi+2-Deoxy-D-glucose

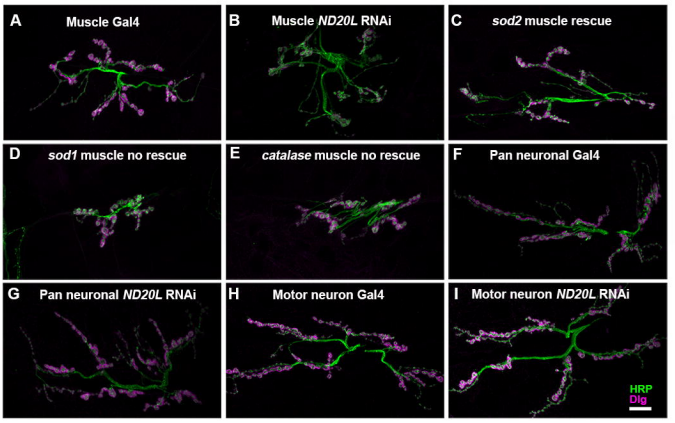
A Muscle Gal4
B Muscle ND20L RNAi
C sod2 muscle rescue
D sod1 muscle no rescue
E catalase muscle no rescue
F Pan neuronal Gal4
G Pan neuronal ND20L RNAi
H Motor neuron Gal4
I Motor neuron ND20L RNAi
HRP
Dlg

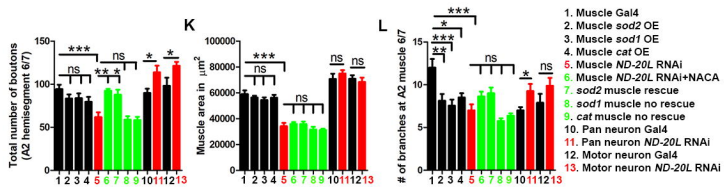
J
Total number of boutons (A2 hemisegment 6/7)
K
Muscle area in µm²
L
# of branches at A2 muscle 6/7
1. Muscle Gal4
2. Muscle sod2 OE
3. Muscle sod1 OE
4. Muscle cat OE
5. Muscle ND-20L RNAi
6. Muscle ND-20L RNAi+NACA
7. sod2 muscle rescue
8. sod1 muscle no rescue
9. cat muscle no rescue
10. Pan neuron Gal4
11. Pan neuron ND-20L RNAi
12. Motor neuron Gal4
13. Motor neuron ND-20L RNAi

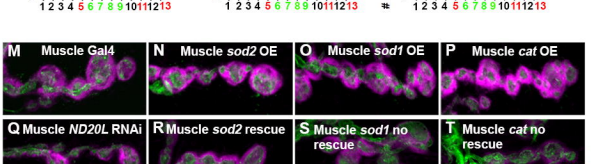
M Muscle Gal4
N Muscle sod2 OE
O Muscle sod1 OE
P Muscle cat OE
Q Muscle ND20L RNAi
R Muscle sod2 rescue
S Muscle sod1 no rescue
T Muscle cat no rescue
HRP
Dlg

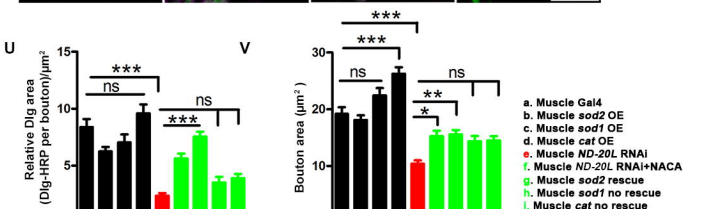
U
Relative Dlg area (Dlg-HRP per bouton)/µm²
V
Bouton area (µm²)
a. Muscle Gal4
b. Muscle sod2 OE
c. Muscle sod1 OE
d. Muscle cat OE
e. Muscle ND-20L RNAi
f. Muscle ND-20L RNAi+NACA
g. Muscle sod2 rescue
h. Muscle sod1 no rescue
i. Muscle cat no rescue

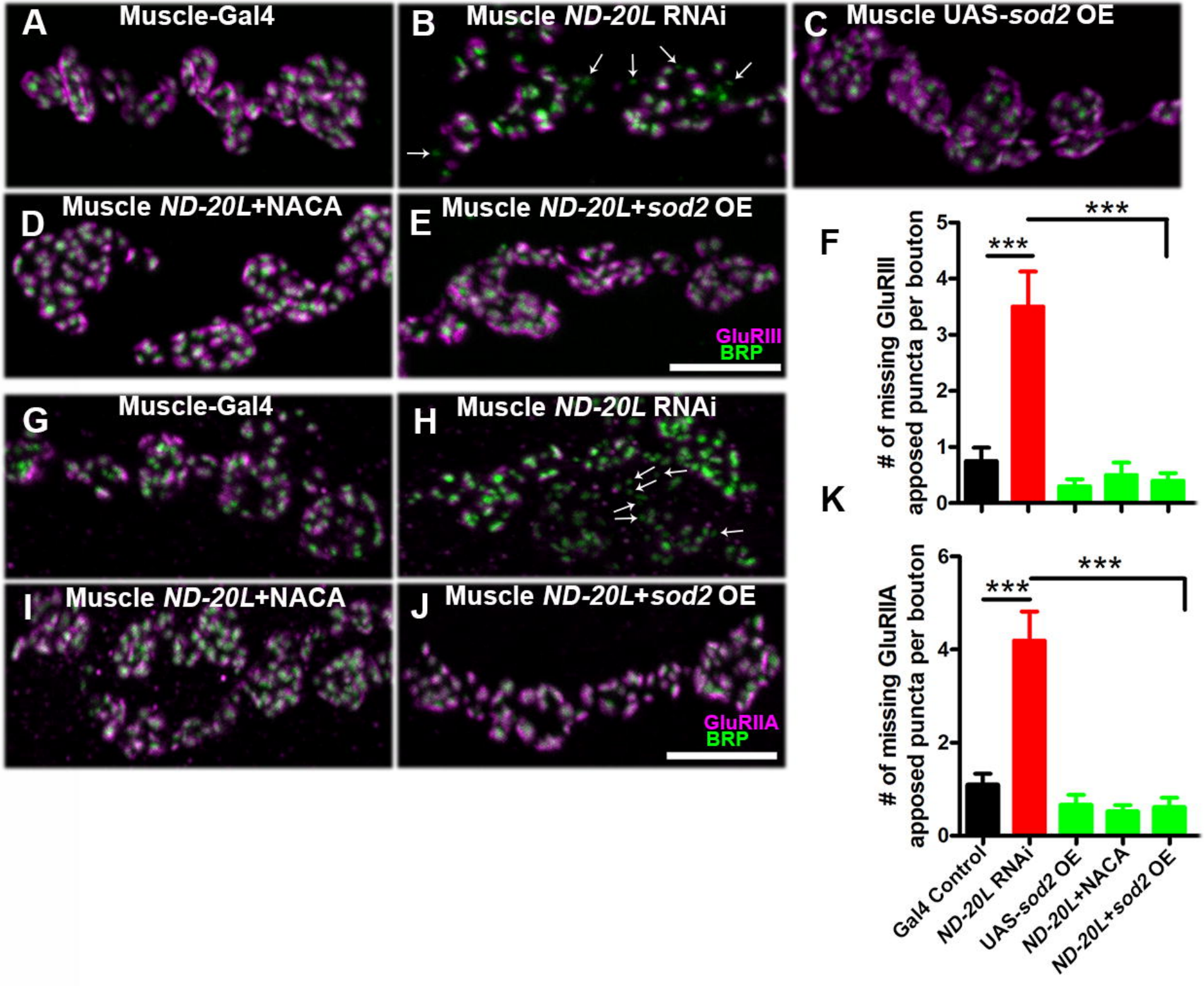
A
Muscle-Gal4
B
Muscle ND-20L RNAi
C
Muscle UAS-sod2 OE
D
Muscle ND-20L+NACA
E
Muscle ND-20L+sod2 OE
GluRIII
BRP
F
# of missing GluRIII apposed puncta per bouton
***
***
0
1
2
3
4
5
G
Muscle-Gal4
H
Muscle ND-20L RNAi
I
Muscle ND-20L+NACA
J
Muscle ND-20L+sod2 OE
GluRIIA
BRP
K
# of missing GluRIIA apposed puncta per bouton
***
***
0
2
4
6
Gal4 Control
ND-20L RNAi
UAS-sod2 OE
ND-20L+NACA
ND-20L+sod2 OE

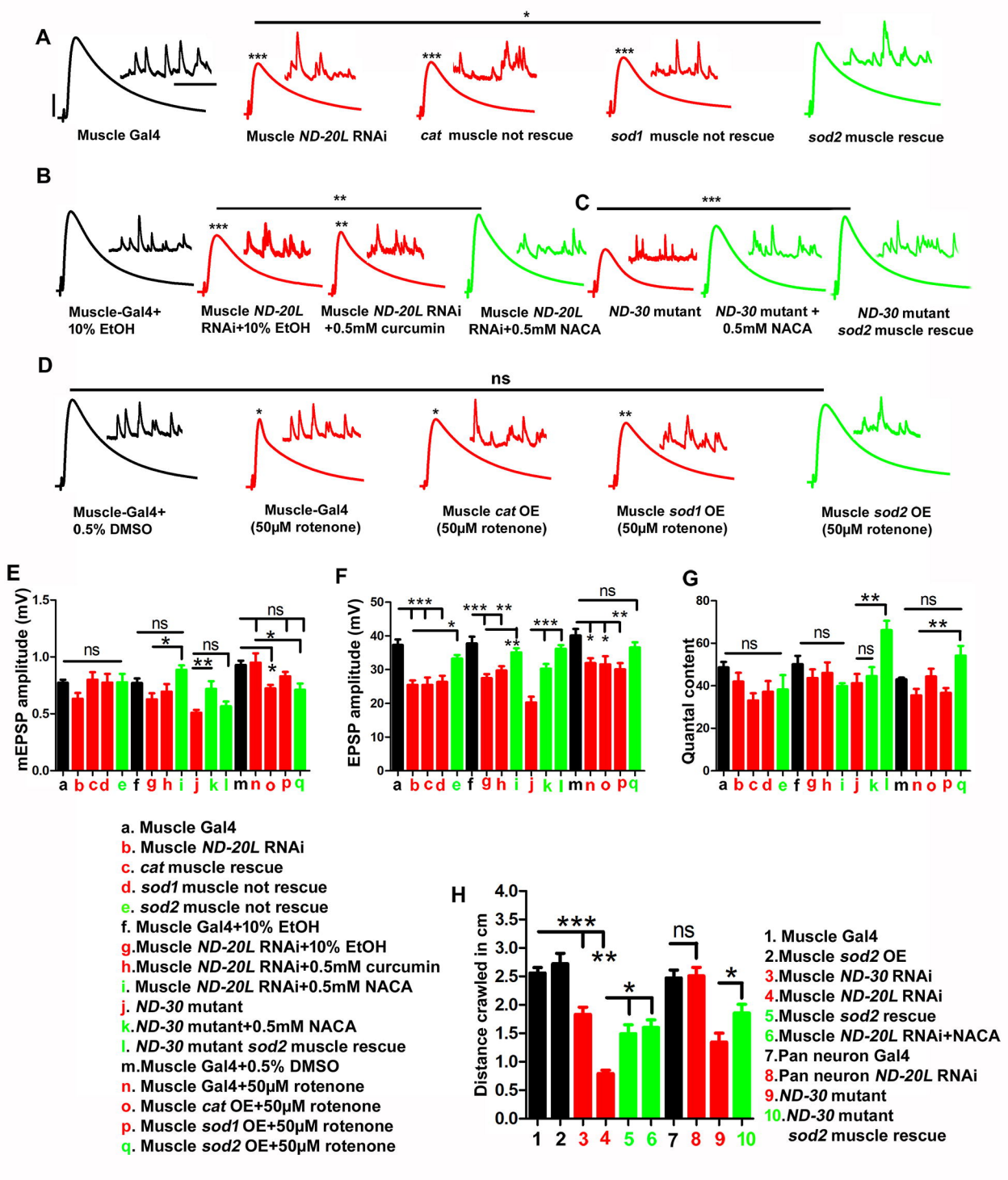
A
Muscle Gal4
Muscle ND-20L RNAi
cat muscle not rescue
sod1 muscle not rescue
sod2 muscle rescue
B
Muscle-Gal4+ 10% EtOH
Muscle ND-20L RNAi+10% EtOH
Muscle ND-20L RNAi +0.5mM curcumin
Muscle ND-20L RNAi+0.5mM NACA
C
ND-30 mutant
ND-30 mutant + 0.5mM NACA
ND-30 mutant sod2 muscle rescue
D
ns
Muscle-Gal4+ 0.5% DMSO
Muscle-Gal4 (50μM rotenone)
Muscle cat OE (50μM rotenone)
Muscle sod1 OE (50μM rotenone)
Muscle sod2 OE (50μM rotenone)
E
mEPSP amplitude (mV)
F
EPSP amplitude (mV)
G
Quantal content
a. Muscle Gal4
b. Muscle ND-20L RNAi
c. cat muscle rescue
d. sod1 muscle not rescue
e. sod2 muscle not rescue
f. Muscle Gal4+10% EtOH
g.Muscle ND-20L RNAi+10% EtOH
h.Muscle ND-20L RNAi+0.5mM curcumin
i. Muscle ND-20L RNAi+0.5mM NACA
j. ND-30 mutant
k.ND-30 mutant+0.5mM NACA
l. ND-30 mutant sod2 muscle rescue
m.Muscle Gal4+0.5% DMSO
n. Muscle Gal4+50μM rotenone
o. Muscle cat OE+50μM rotenone
p. Muscle sod1 OE+50μM rotenone
q. Muscle sod2 OE+50μM rotenone
H
Distance crawled in cm
1. Muscle Gal4
2.Muscle sod2 OE
3.Muscle ND-30 RNAi
4.Muscle ND-20L RNAi
5.Muscle sod2 rescue
6.Muscle ND-20L RNAi+NACA
7.Pan neuron Gal4
8.Pan neuron ND-20L RNAi
9.ND-30 mutant
10.ND-30 mutant sod2 muscle rescue